THESIS FOR THE DEGREE OF DOCTOR OF PHILOSOPHY

Numerical prediction of propeller induced hull pressure pulses and noise

Muye Ge

Department of Mechanics and Maritime Sciences
CHALMERS UNIVERSITY OF TECHNOLOGY
Göteborg, Sweden 2021

Numerical prediction of propeller induced hull pressure pulses and noise

MUYE GE
ISBN: 978-91-7905-586-8

Series number: 5053
ISSN 0346-718X

Department of Mechanics and Maritime Sciences
Chalmers University of Technology
SE-412 96 Göteborg
Sweden
Telephone + 46 (0)31-772 1000

Printed by Chalmers Reproservice
Göteborg, Sweden 2021

Numerical prediction of propeller induced hull pressure pulses and noise

MUYE GE, 2021
Department of Mechanics and Maritime Sciences, Chalmers University of Technology

Abstract

An operating marine propeller is one of the major sources inducing hull pressure pulses, onboard noise and vibration as well as underwater radiated noise. There are rising concerns of environmental impacts and comfort and welfare of passengers and crews due to these negative effects. Cavitation is a significant source of these effects, but it is typically inevitable if only the hydrodynamic efficiency of the propeller is optimized. To reduce the noise and the pressure pulses caused by the cavitation, a trade-off of the hydrodynamic efficiency should be made to design and optimize a propeller that possess both high hydrodynamic performance and low noise and hull pressure pulse generation. More accurate predictions are needed to identify the best trade-off between a high efficiency propeller design and a low pressure pulse and noise one.

The study focuses on the numerical prediction of hull pressure pulses and radiated underwater noise using viscous CFD including the opensource package OpenFOAM and commercial package Star-CCM+. Numerical predictions are performed regarding different experimental configurations for determining hull pressure pulses and ship noise, including propellers mounted on inclined shafts and propellers operating behind ship hulls, under different scales and scaling laws with different operating conditions and Reynolds numbers.

Non-cavitating propeller induced pressure pulses are generally lower in levels and rich in blade passing frequency comparing to cavitating conditions, with blade tip clearance as a major impact factor. For cavitating conditions the rate of cavity growth/shrinkage is found to play the dominating role generating pressure fluctuations. For certain model scale configurations, numerical predictions with ordinary approaches predict massive sheet cavity on propeller blades leading to pressure pulse prediction discrepancies comparing to experimental observations and measurements. These can be significantly improved by a developed bridged model considering laminar to turbulence transition. Tip vortex cavitation bursting is a common phenomenon found on propellers operating behind the ship hull and generating significant levels of pressure pulses. The phenomenon is numerically predicted with investigations of its generation mechanisms in relation to the propeller inflow, convex shaped sheet cavitation closure line and traveling re-entrant jet underneath the sheet cavity.

Propeller induced noise prediction was studied using approaches focused on the FWH (Ffowcs Williams-Hawkings) acoustic analogy with incompressible input on permeable/porous data surface (PDS). Studies show this combination between incompressible input and FWH acoustic analogy can be erroneous, though using certain PDS placements and closer receivers the error can be reduced.

Keywords: Cavitation, Pressure pulses, Ship noise, FWH acoustic analogy, Hydroacoustics, Sheet cavitation inception, RANS, IDDES, $k-\omega$ *SST*, Transition.

ACKNOWLEDGEMENT

First of all, I would like to express my gratitude to my main supervisor and examiner Professor Rickard E. Bensow. Thank you very much for picking me up into this research field and your granted freedom to explore. Your continuous supports and immense knowledge always guide my way, especially when I got lost. Thank you very much for your patience, understanding and kindness during my days under pressure. Thank you, for everything, and sorry for the times I was being childish.

Many thanks to my co-supervisor, Dr. Urban Svennberg, for his valuable supports, encouragement and shared experiences. I don't know how to express my gratitude to you; I am so lucky to have you as my supervisor as well. In addition, I would like to thank Dr. Marko Vikström for your always supports and discussions.

I would like to express my gratitude to Johan Lundberg and Göran Grunditz for their supports and encouragement throughout the research project and involvement in the research details. Thank you very much for the opportunities and I really like the discussions during our meetings.

Thank you all very much for the always kindness. You all gave me much more than I deserve.

I would like to thank Professor Jonas Ringsberg, the head of Marine Technology division, for his supports and for providing a perfect working environment. Special thanks to my colleagues in the division, for the times we had during meetings, lunches and coffee breaks. It has been a pleasure to work with all of you.

Financial support for this work has been provided by Kongsberg Maritime Sweden AB through the University Technology Centre in Computational Hydrodynamics hosted at the Department of Mechanics and Maritime Sciences at Chalmers University of Technology. The computations were performed on resources at Chalmers Centre for Computational Science and Engineering (C3SE) and National Supercomputer Centre (NSC) at Linköping University provided by the Swedish National Infrastructure for Computing (SNIC).

LIST OF PAPERS

The thesis consists of the following publications:

Paper A M. Ge, U. Svennberg, and R.E. Bensow. Investigation on RANS prediction of propeller induced pressure pulses and sheet-tip cavitation interactions in behind hull condition. Ocean Engineering, 2020, 209: 107503.

Paper B M. Ge, U. Svennberg, and R. E. Bensow. Numerical investigation of pressure pulse prediction for propellers mounted on an inclined shaft. In Sixth International Symposium on Marine Propulsors, Rome, Italy, 2019.

Paper C M. Ge, U. Svennberg, and R. E. Bensow. Numerical investigation of propeller induced hull pressure pulses using RANS and IDDES. In IX International Conference on Computational Methods in Marine Engineering, Edinburgh, Scotland, UK, 2021.

Paper D M. Ge, U. Svennberg, and R. E. Bensow. Improved sheet cavitation inception prediction using bridged transition sensitive turbulence model and cavitation model. Submitted to Journal of Marine Science and Engineering.

Paper E M. Ge, U. Svennberg, and R. E. Bensow. Investigations on prediction of ship noise using the FWH acoustic analogy with incompressible flow input. Submitted to Ocean Engineering.

Contribution: In the list papers, the author of the thesis contributed in the planning of the work, performing numerical simulations, analysis and post-processing of the numerical results and writing original draft . Urban Svennberg contributed experimental measurements of the Kongsberg propellers in paper B and paper D, writing-review & editing and project administration. Rickard. E. Bensow contributed in conceptualization, writing-review & editing, resources and project administration.

OTHER RELEVANT PUBLICATIONS

In addition to the appended papers, I have authored or co-authored the following publications during my PhD:

Paper I R. E. Bensow, M. Ge, M. Irannezhad, and A. Eslamdoost. D9.6, CFD report of Large Diameter Propeller for General Cargo Vessel. In project of Low Energy And Near to zero emissions Ships (LeanShips), 2019.

Paper II M. Ge, S. Wu, M. Hyensjö, and R. E. Bensow. Computational analysis of two correlation based transition-sensitive models on a model scale marine propeller. 12th International OpenFOAM Workshop, Exeter, UK, 2017.

Paper III M. Ge, and R. E. Bensow. Comparison of Free Surface Capturing Approaches in OpenFOAM for Ship Resistance Prediction, 20th Numerical Towing Tank Symposium, Wageningen, Neitherland, 2017.

Paper IV M. Ge, U. Svennberg, and R. E. Bensow. Investigation on Numerical Prediction of Propeller Induced Hull Pressure Pulses. 10th International Symposium on Cavitation (CAV2018), Baltimore, Maryland, USA, 2018.

Paper V M. Ge, U. Svennberg, and R. E. Bensow. Numerical investigation of tip vortex bursting and induced hull pressure pulses on a container vessel. 11th International Symposium on Cavitation (CAV2021), Daejeon, Korea, 2021.

Paper VI M. Ge. Numerical prediction of propeller induced hull pressure pulses. Technical report, Department of Mechanics and Maritime Sciences, Chalmers University of Technology, 2019. Lic. Eng, Thesis, Report no 2019:12.

CONTENTS

1

Introduction

Shipping is the most economical way of freight transportation and contributes to the majority of world trade of cargo. As a major approach of ship propulsion, marine propellers are widely used and propeller design with high propulsion efficiency is the major quest for propeller designers. However, there are several side-effects generating design constraints including induced hull pressure pulses and radiated noise which have been getting more attention in recent years.

High levels of on-board vibration and noise can impose health hazards to the seafarers who are long-term exposed, including change of hearing sensitivity, resonance in air containing organs, disorientation and acoustic annoyance [1]. Regulations like IMO Resolution MSC.337 addresses limits of on-board noise levels at different on-board areas according to exposure hours. The arising market of cruise vessels and yachts also require noise and vibration below certain levels to maintain the comfort of passengers as the pressure fluctuation on the hull body above the propeller is one of the major sources of hull vibrations.

Ship noise radiation has been drawing more and more attention and it has been shown that the ship noise pollution levels almost doubled every decade during year 1960-2000 [1] and according to [2] this trend is not slowing down. Shown in [3] there is an overlap between low frequency noise radiated by marine vessels and whale communication signals, which lead to a series of health hazard for these sea mammal. Especially, the low frequency noise at several blade passing frequencies could travel as far as hundreds of kilometers. The acoustic pollution potentially influence the underwater environments and marine wildlife [4]; e.g. quite concretely, it has been shown how a blue whale was trying to avoid commercial vessels [5]. The arctic transportation path is a new hot spot. The existence of ice cover may change the propagation properties of generated noise, and the impacts to arctic environments can be another constraint.

In recent years, regulations, standards and rules have been developing. ISO has provided detailed information for standardised noise measurement and com-

parison for full scale operating vessels under various conditions [6, 7]. Similar standards can be found in [8, 9, 10] as well as the regulations by ship classification societies and rules, including [11] and [12] in which silent classes or noise marks for vessels are defined. Recent detailed reviews and discussions regarding the topic can be found in [13] and [14].

Marine propellers are typically operating behind the hull body inside the ship wake. By the propeller blades rotational motion, pressure differences are created on the two sides of a blade and generating thrust force. The field spatial distribution change of pressure also generates pressure waves to the surrounding medium, which is one of the major sources of hull vibration, on-board noise and under-water noise. The pressure on the propeller blades can also drop below water saturation pressure and tension force break the water medium, known as cavitation, which contributes significantly to these side effects.

Cavitation can be classified into traveling bubble cavitation, attached sheet cavitation and vortex cavitation [15], and shown in figure 1.1 on a model scale marine propeller. Tip vortex cavitation is usually the first cavitation phenomenon and its appearance, referring to tip vortex cavitation inception, lead to significant increase of hull pressure pulses and noise levels. Sheet cavitation can be typically found attached on the blade suction side as a rolling structure with a larger extent. Traveling bubble cavitation with single developed bubble, as shown in figure 1.1, is widely found on mid-blades in model scale experiments but rarely observed on full scale ships.

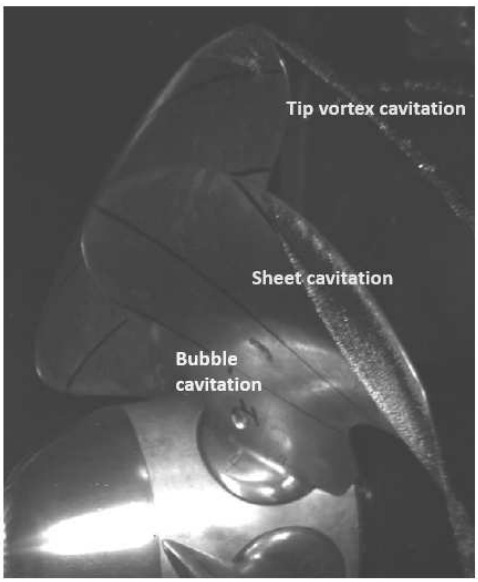

Figure 1.1: Typical cavitation phenomenon on propeller blades.

1.1 Full scale measurements and experimental procedures

Hull pressure pulses and radiated noise levels can be measured via full scale ship sea trails. Especially regarding under-water radiated noise (URN), typically the full scale vessel need to be tested in the open sea with required water depth, and single or multiple hydrophones with different possible deployments at far-field (1 - 2 times ship overall length) are used to collect the noise data, and the Sound Pressure Level (*SPL*) measured by the hydrophones will be corrected and scaled to the noise source level (*Ls*) equivalent at 1 m distance using formulations based on distance normalization of spherical wave spreading or similar. *Ls* can be shown in 1/3 octave band spectrum and according to the classification rules, the *Ls* are required to be below a certain threshold.

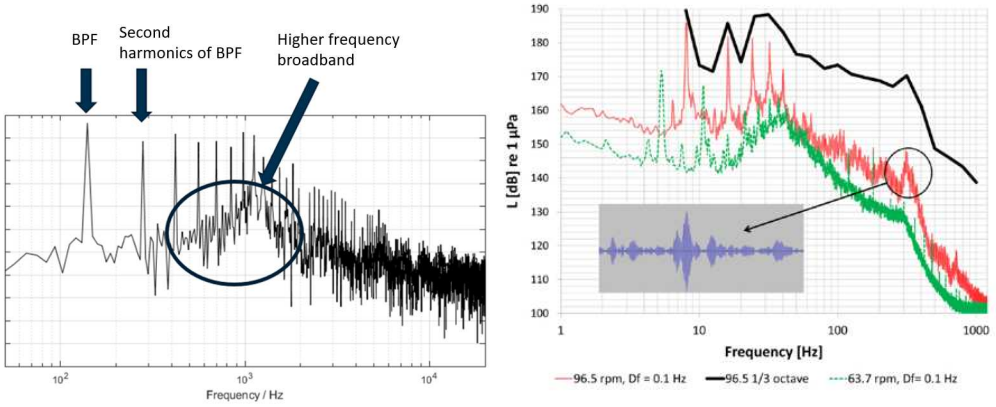

(a) Model scale *Ls* in narrowband

(b) Full scale *Ls* in narrowband and in 1/3 octave bands [16]

Figure 1.2: Typical ship noise source level spectrum.

The propeller induced hull pressure pulses and noise are quite in phase with the blade's rotational motion, thus the levels are commonly shown in harmonics of blade passing frequency (BPF) and fast Fourier transformation (FFT) is widely used to analyze the levels in frequency domain. Typical ship noise source levels *Ls* can be found in figure 1.2 for model scale and full scale ships. The spectra have clear peaks which are located at higher harmonics of BPF. As a general picture, for full scale ships, the propeller rotation speeds are typically between 60 - 120 *rpm*; assuming a five-bladed propeller the blade passing frequency corresponds to 5 - 10 Hz. For model scale propellers tested in the cavitation tunnel, the rotation speeds are commonly adjusted to around 20 *rps*, resulting in BPF around 100 Hz. For model scale propellers operating in a self-propulsion test following Froude's scaling law, the rotation speeds are usually between 5 - 10 *rps*, resulting in BPF around 25 - 50 Hz. A central hump with relatively high levels of broadband noise can be found in figure 1.2 as well, with central frequency usually located between third to tenth harmonics of BPF.

Model scale experiments can be performed for the determination of hull pressure pulses and ship radiated noise before the real ship is built. Experiments are usually performed in facilities that can be depressurized to the required cavitation number σ to trigger cavitation. Propeller Openwater Test (POT) are typically used to determine a propeller's propulsion characteristics, in which the model scale marine propeller is operating under uniform inflow. Within a small-size and medium-size cavitation tunnel, the pressure inside the tunnel can be depressurized to the desired σ and pressure pulses or radiated noise can be measured, typically via wall mounted transducers and hydrophones inside the tunnel. But this type of configuration has several drawbacks and the major problem is that in real vessels, propellers are operating in the ship wake and the blade pressure and cavitation pattern are changing with the spatial distribution of the wake strength. This non-uniform propeller inflow is an important factor. Under uniform propeller inflow, cavitation will be relatively steady with small variations of sheet cavitation and tip vortex cavitation, and steady cavity structures are usually harmless regarding pressure pulses and noise [17]. With this uniform inflow configuration the pressure pulses and noises are mainly induced by relatively weaker tip vortex dynamics and collapse of small vapor structures, and the significant pressure pulse and noise levels induced by sheet cavitation variations and related tip vortex cavitation dynamics are missed in this type of configuration. In order to create a more relevant propeller inflow, the propeller may be mounted on an inclined shaft or tested with upstream panels and meshes, inside a medium-size cavitation tunnel. The model scale ship hull can also be mounted inside a large-size cavitation tunnel or a large wave basin that can be depressurized, with the propeller operating behind the hull. Pressure pulses can be measured via transducers mounted on the hull body and noise measurements can be achieved via different deployments, including hydrophone(s) beside the operating propeller, downstream the propeller, outside the propeller wake disc, inside an acoustic chamber connected to the test section and mounted fitted to a mast inside the wave basin.

Measured model scale hull pressure pulses can be scaled to full scale levels using non-dimensional scaling, but the measured noise signal by deployed hydrophones need to be corrected to get model scale or full scale ship noise level. Apart from the procedures needed to calibrate background noise, the transmission loss TL needs to be calibrated especially inside cavitation tunnels due to complex reflection and reverberations [18, 19], while for real cases the ship and propeller are operating in the open sea with hydrophones placed at far-field. The model scale ship noise source level Ls can then be scaled to full scale levels, according to scaling rules; these may also differ between different institutes. General experimental procedure guidelines can be found in recommendations in [20].

1.2 NUMERICAL ASSESSMENT

Numerical prediction of pressure pulses and ship noise can be classified with increasing computational cost as empirical approach, potential flow based approach and viscous flow based approach. The empirical approach could also be used together with other approaches and these blended approaches are referred to as semi-empirical approaches. For the potential flow based approach, Boundary Element Method (BEM), lifting line method, lifting surface method and other techniques can be found widely used. For the viscous flow based approach, RANS (Reynolds-Averaged Navier-Stokes) and LES (Large Eddy Simulation) as well as the combination between the two, DES (Detached Eddy Simulation), can be commonly found. The potential flow based approach and viscous flow based approach could be used separately or together to balance computational cost and accuracy. Besides, data driven models are also emerging [21]. The prediction of noise can be achieved via direct simulation using a compressible solver with very high demand of computational resources, and the use of acoustic analogies with flow input using various codes are being investigated for ship noise prediction in recent years.

1.3 OBJECTIVES

The research is focused on giving the scientific foundation for an engineering tool for prediction of pressure pulses and under-water radiated noise induced by operating propellers. Marine propeller induced pressure pulses and noise are often required in contract to be below a certain level. More accurate pressure pulse and noise predictions would make it possible to reduce the margin between a high performance design and a low pressure pulse and noise design.

In order to achieve the research objectives, the following cases are studied:

- A general cargo vessel with LDP

  The first studied case is a general cargo vessel designed and studied in the LeanShips EU project which attempts to acquire maximum propeller efficiency by using a large diameter propeller (LDP) incorporated by a new hull design with significantly reduced tip clearance. The tip clearance is about 1% of propeller diameter, much smaller than the typical choices of 20% $\sim$ 30% of propeller diameter, and induced pressure pulse levels became one of the major concerns to be taken care of. Both model scale and full scale simulations were performed and the first to fourth harmonics pressure pulses were predicted and compared to experimental measurements. Besides, the effect of hull roughness was also studied. The study revealed the importance of tip clearance regarding hull pressure pulse levels, discussed the differences between model scale and full scale configurations, and the mechanism of higher harmonics pressure pulse generations by spike-like signals.

- Open-water propellers on inclined shaft

  Numerical simulations regarding two high-skew model scale marine propellers mounted on inclined shaft were performed and pressure pulses at blade frequency were investigated. Simulations were conducted under different operating conditions J and cavitation numbers σ. Several meshes were generated systematically and used to perform a mesh dependency study. However, massive sheet cavitation were predicted by both Star-CCM+ and OpenFOAM on the propeller blades, while in the high speed videos recorded during the experiments the sheet cavitation is limited in size with intermittent cavitation strips or bubble cavities at the over-predicted regions. The significant discrepancies between cavitation patterns observed in experiments and predicted in numerical simulations lead to significant difference of pressure pulse levels. To overcome the issue a bridged model considering laminar to turbulence transition was developed and applied on the two propellers with improved predictions. Besides, the widely studied propeller VP1304 was studied as well, which was tested during the 2^{nd} SMP workshop [22] where massive sheet cavitation were commonly predicted by various participants.

- NACA16012 hydrofoil

  The NACA16012 hydrofoil was studied to understand the sheet cavitation suppression phenomenon by laminar-transitional boundary layer and to develop a bridged model between a correlation based transition turbulence model and a mass transfer model. The bridged model predicted significantly improved sheet cavitation prediction compared to the unbriged model and agreed very well compared to experimental observations.

- A conventional container vessel

  The studied case is the container vessel designed and studied in the VIRTUE and SONIC EU projects. In the experiments performed at HSVA, the model scale ship hull was put into the cavitation tunnel test section, thus the propeller was operating in a ship wake. Noise measurements were performed via a hydrophone mounted inside an acoustic chamber connected to the test section. Wake prediction was studied by several generated meshes for the ship hull region. Two meshes with/without blade tip refinements were considered to study tip vortex cavitation related phenomenon. Several configurations based on different scaling with different operating Reynolds numbers were numerically considered. For hull pressure pulse predictions, both Star-CCM+ and OpenFOAM were used for cross-reference and compared to experimental measurements; both RANS and IDDES were used in Star-CCM+ regarding hull pressure pulses and noise predictions. Noise predictions were achieved via different approaches including different usages of FWH acoustic analogy.

1.4 MAIN FINDINGS

The major findings in the project are

- Mechanisms of tip vortex bursting, which induce high levels of hull pressure pulses. The phenomenon is referred to "destruction of tip vortex cavitation by re-entrant flow in the sheet cavitation" in [23]. It is one of the common phenomenon on ship propellers and can be related to the traveling re-entrant jet under-neath the sheet cavity, and its formation is related to the convex shaped sheet cavity closure line and the spatial distribution of propeller inflow.

- A numerical model has been developed that bridges the mass transfer cavitation model and transition sensitive turbulence model. The massive overprediction of sheet cavitation on model scale marine propellers operating in relatively uniform inflow is widely reported in many studies; and it is known in model scale tests the cavitation patterns may differ between different test facilities for the same tested geometries and operating conditions. Apart from the nuclei content in the water medium, the study shows that the sheet cavitation inception influenced by possible laminar separation is a major factor. The bridged model predicted significantly improved sheet cavitation pattern on the studied hydrofoil and propellers comparing to the unbridged ordinary approach.

- Ship noise was predicted with the FWH acoustic analogy, using incompressible flow input and porous/permeable data surface (PDS). The use of $PDS-FWH$ has been investigated in recent years, considering the large portion of cavities away from propeller surfaces but generating significant noise which can be difficult to be included in the $S-FWH$ (FWH acoustic analogy with input on impermeable data surface) approach. Incompressible solution is widely used due to reasons including the complexity and high computational demands with compressible solution. The work uses incompressible solution input for FWH acoustic predictions and in certain combinations odd predictions are noticed; a representative free-field monopole representing the predicted cavity on propeller blades are designed and tested with different placements of PDS and with input of both incompressible and compressible solutions. The conclusion is that incompressible solution can be erroneous; the error can be made small with certain combinations, but for ship far-field noise predictions with cavitating propeller, there is no such PDS with neglectable errors.

1.5 THESIS OUTLINE

Following the present chapter, the thesis is structured as follows:

In Chapter 2, the governing equations employed in the current study for numerical simulations are presented. The major studied cases are described in Chapter 3. The pressure pulse predictions for non-cavitating conditions are summarized in Chapter 4. The sheet cavitation inception related studies are summarized in Chapter 5. Predictions of cavitation and induced hull pressure pulses are presented in Chapter 6. The predictions of propeller induced noise are summarized in Chapter 7 including discussions of noise predictions for a designed free-filed monopole test case. The work is summarized in Chapter 8.

The appendix includes the prepared/published papers, where further details about the literature review, methodologies, and cases studied are presented.

2

Governing equations

2.1 Mass and momentum continuity equation

The basic control equations used in the present study are the mass continuity equation and momentum continuity equation, and their formulation in URANS for incompressible flow is

$$\frac{\partial \rho_m}{\partial t} + \nabla(\rho_m \overline{\mathbf{U}}) = 0, \tag{2.1}$$

$$\frac{\partial \rho_m \overline{\mathbf{U}}}{\partial t} + \overline{\mathbf{U}} \cdot \nabla(\rho_m \overline{\mathbf{U}}) = \nabla \cdot (\overline{\tau} - \tau_{RANS}) - \nabla \overline{p} + F_s, \tag{2.2}$$

and the Boussinesq hypothesis is used for Reynolds stress tensor τ_{RANS} modeling,

$$\tau_{RANS} = -\rho_m \overline{\mathbf{U}'\mathbf{U}'} = \mu_t(\nabla \overline{\mathbf{U}} + (\nabla \overline{\mathbf{U}})^T) - \frac{2}{3}\rho_m k \mathbf{I}, \tag{2.3}$$

in which μ_t is turbulent viscosity, F_s represents body forces, ρ_m for mixture density, $\overline{\tau}$ represent averaged stress tensor and $\mathbf{I}$ represents identity tensor. The turbulent viscosity can be modelled using the $k-\omega$ *SST* turbulence model as $\mu_t = \frac{\rho_m k}{\omega} \frac{1}{max[1/\alpha^*, SF_2/a_1\omega]}$ where α^*, a_1 are model constants, S is the strain rate magnitude, F_2 is a blending function and k and ω represent kinetic energy and specific dissipation rate respectively and both k and ω are modeled via Reynolds transport equations. The implementation of $k-\omega$ *SST* in Star-CCM+ is based on [24] with modifications [25] and for the implementation in OpenFOAM is based on [26] with updated coefficients [27]. In OpenFOAM, wall functions are used for k, ω and ν_t typically for full scale simulations or in regions of less interest, e.g. model scale tunnel section walls. In most model scale simulations the wall functions are typically not used in regions of importance with $y+ < 1$ where on the wall surfaces k and ν_t are set to 0 with ω treated using the compound wall treatment [28]. In Star-CCM+, the blended all $y+$ wall treatment is used [25].

As a hybrid between RANS and LES, IDDES takes the computational advantages of RANS for boundary layer flow and achieves better accuracy using LES for unsteady separated regions. For hybriding, the momentum equation can be written as shown in equation 2.4 dependent on the local definition,

$$\frac{\partial \rho_m \hat{\mathbf{U}}}{\partial t} + \hat{\mathbf{U}} \cdot \nabla(\rho_m \hat{\mathbf{U}}) = \nabla \cdot (\hat{\tau} - \tau_{model}) - \nabla \hat{p} + F_s, \tag{2.4}$$

in which the modeled stress tensor τ_{model} is defined as $\tau_{model} = f_\Delta(\frac{\Delta}{l_k})\tau_{RANS}$, where Δ represents the local measure of the grid size, l_k represents turbulent length scale and f_Δ is a damping function. Together with $k-\omega$ SST, the transport equation for k is modified to

$$\frac{\partial \rho_m k}{\partial t} + \nabla \cdot (\rho_m \hat{\mathbf{U}} k) = \nabla \cdot [(\mu_m + \sigma_k \mu_t)\nabla k] + P_k - \rho_m \sqrt{k^3}/l_{IDDES}, \tag{2.5}$$

where the IDDES length scale l_{IDDES} can be obtained with RANS length scale $l_{RANS} = \sqrt{k}/(C_\mu \omega)$ and LES length scale $l_{LES} = C_{DES}\Delta_{IDDES}$, together with a delaying function $\tilde{f}_d$ and an evaluating function f_e as

$$l_{IDDES} = \tilde{f}_d \cdot (1 + f_e) \cdot l_{RANS} + (1 - \tilde{f}_d) \cdot l_{LES}. \tag{2.6}$$

In Star-CCM+, mesh length scale δ_{IDDES} is calculated as

$$\Delta_{IDDES} = \min(\max(0.15d, 0.15\Delta, \Delta_{min}), \Delta), \tag{2.7}$$

in which d represents wall distance, Δ and Δ_{min} represent the largest and smallest distance between the cell center under consideration and the cell centers of the neighboring cells. The details of IDDES formulations can be found in Star-CCM+ documentation [25] based on [29].

Cavitation is one of the major sources of propeller induced pressure pulses. The single fluid linear mixture approach is used for the present multi-phase problem. The two phases water and vapor are represented by a volume fraction factor α which is between 0 and 1 thus the mixture properties could be calculated as

$$\rho_m = \alpha_l \rho_l + (1 - \alpha_l)\rho_v, \quad \mu_m = \alpha_l \mu_l + (1 - \alpha_l)\mu_v, \quad \alpha_l + \alpha_v = 1,$$

in which the subscripts l and v represent liquid phase related quantities and vapor phase related quantities. The transport equation of the volume fraction could be written as a purely convection equation with mass transfer source term for the liquid phase,

$$\frac{\partial \alpha_l}{\partial t} + \nabla \cdot \alpha_l \mathbf{U} = \frac{\dot{m}}{\rho_l}. \tag{2.8}$$

2.2 SCHNERR-SAUER CAVITATION MODEL

In reality, rather than a perfect purified medium, water contains imperfections and the small bubbles are one of the major sources to break the water medium when under tension. The small bubbles are also referred to as nuclei. The information of nuclei including the distribution of numbers and sizes can be determined experimentally, and usually it differs from test to test.

As mentioned earlier, the FVM-based approaches rely on cavitation models to simulate the process. There are many cavitation mass transfer models available, and the Schnerr-Sauer cavitation model is one of the widely used models. For the study regarding marine propeller cavitation, the difference between different phase change modeling approaches are not expected to be significant [30]. In the Schnerr-Sauer cavitation model [31], the distribution of nuclei are assumed to be spherical and uniformly distributed in the water medium. For uniformly distributed nuclei with diameter d and number n the volume in one unit can be estimated as in Equation 2.9, thus the volume fraction of nuclei can be expressed as in Equation 2.10, and bubble growth rates could be estimated using a simplified Rayleigh relation as shown in Equation 2.11,

$$V_{nuc} = \frac{1}{6} n \pi d^3, \tag{2.9}$$

$$\alpha_{nuc} = \frac{V_{nuc}}{1 + V_{nuc}} = \frac{\frac{1}{6} n \pi d^3}{1 + \frac{1}{6} n \pi d^3}, \tag{2.10}$$

$$\frac{dR}{dt} = \sqrt{\frac{2}{3} \frac{p_{sat} - p_{\infty}}{\rho_l}}. \tag{2.11}$$

Accordingly, the vapor production rate can be calculated as

$$\frac{d\alpha}{dt} = (1 - \alpha) \frac{4 \pi n R^2 \frac{dR}{dt}}{1 + 4 \pi n R^3 / 3}. \tag{2.12}$$

The source mass transfer term on the right hand side of Equation 2.8 can be further re-organized as shown,

$$\frac{\dot{m}}{\rho_l} = \frac{\dot{m}}{\rho_l} - \alpha_l (\frac{1}{\rho_l} - \frac{1}{\rho_v}) + \alpha_l (\frac{1}{\rho_l} - \frac{1}{\rho_v}) = (\frac{1}{\rho_l} - \alpha_l (\frac{1}{\rho_l} - \frac{1}{\rho_v})) \dot{m} + \alpha_l (\frac{1}{\rho_l} - \frac{1}{\rho_v}) \dot{m}, \tag{2.13}$$

while the first term in Eq. 2.13 on the right hand side can be decomposed into two terms (one for vaporization and one for condensation) as

$$\dot{m}_{ac} = C_c \alpha_l \frac{3 \rho_l \rho_v}{\rho_m R} \sqrt{\frac{2}{3 \rho_l}} \sqrt{\frac{1}{|p - p_{threhold}|}} \max(p - p_{threhold}, 0),$$

$$\dot{m}_{av} = C_v(1+\alpha_{nuc}-\alpha_l)\frac{3\rho_l\rho_v}{\rho_m R}\sqrt{\frac{2}{3\rho_l}}\sqrt{\frac{1}{|p-p_{threhold}|}}\min(p-p_{threhold},0).$$

Then the total rate of mass transfer can be modified accordingly as

$$\dot{m} = \alpha_l\dot{m}_{av} + (1-\alpha_l)\dot{m}_{ac} = \alpha_l(\dot{m}_{av}-\dot{m}_{ac}) + \dot{m}_{ac}. \tag{2.14}$$

By introducing $\dot{V} = (\frac{1}{\rho_l} - \alpha_l(\frac{1}{\rho_l}-\frac{1}{\rho_v}))$ and $\frac{\partial u_i}{\partial x_i} = (\frac{1}{\rho_l}-\frac{1}{\rho_v})\dot{m}$, the final transport equation can be written,

$$\frac{\partial\alpha_l}{\partial t} + \nabla\cdot(\alpha_l\mathbf{U}) = (\nabla\cdot\mathbf{U} + \dot{V}_v - \dot{V}_c)\alpha_l + \dot{V}_c. \tag{2.15}$$

2.3 SEPARATION INDUCED TRANSITION IN THE $\gamma - Re_\theta$ MODEL

The $\gamma - Re_\theta$ transition model based on Local Correlation based Transition Modelling (LCTM) links empirical transition correlations and local determined flow quantities, and is capable in predicting natural transition, bypass transition and separation induced transition. Another two transport equations are used in addition to the coupled turbulence model, with one for intermittency γ and the other for transition momentum thickness Reynolds number $Re_{\theta t}$,

$$\frac{\partial\rho_m\gamma}{\partial t} + \nabla\cdot(\rho_m\mathbf{U}\gamma) = P_\gamma - E_\gamma + \nabla\cdot((\mu_m + \frac{\mu_t}{\sigma_f})\nabla\gamma), \tag{2.16}$$

$$\frac{\partial\rho_m\overline{Re_{\theta t}}}{\partial t} + \nabla\cdot(\rho_m\mathbf{U}\overline{Re_{\theta t}}) = P_{\theta t} + \nabla\cdot(\sigma_{\theta t}(\mu_m+\mu_t)\nabla\overline{Re_{\theta t}}), \tag{2.17}$$

in which P_γ and E_γ represent the production and destruction terms of γ, $P_{\theta t}$ is the production term in the $\overline{Re_{\theta t}}$ equation and σ_f and $\sigma_{\theta t}$ are model constants. The fundamental concept of the transition model is to relate the scaled ratio of vorticity Reynolds number $Re_v = \frac{\rho y^2}{\mu}S$ and the momentum thickness Reynolds number Re_θ, to the boundary layer shape factor H as $\frac{\max(Re_v)}{C\cdot Re_\theta} \sim H$. The constant C equals 2.193 for moderate pressure gradients ($2.3 < H < 2.9$) and equals 3.235 for strong adverse pressure gradients especially near separation ($H = 3.5$). More details about the transition model can be found in [32] and [33], and here only the related part used in the present study will be discussed. Most correlations are considered in the $\overline{Re_{\theta t}}$ equation and when the criteria are satisfied and transition starts, source terms in the γ equation will be activated and γ will increase locally inside the boundary layer. Besides, the separation induced transition, γ_{sep} is calculated separately based on $\frac{\max(Re_v)}{C\cdot Re_{\theta c}} - 1$ with the constant $C = 3.235$ as

$$\gamma_{sep} = \min(s_1\max[0,(\frac{Re_v}{C\cdot Re_{\theta c}}) - 1]F_{reattach}, 2.0)F_{\theta t}, \tag{2.18}$$

while in which s_1 is a model constant, the blending function $F_{reattach}$ controls the boundary layer reattachment and the blending function $F_{\theta t}$ is equal to 0 in the free stream and 1 in the boundary layer, which is used to limiting the γ_{sep} inside the boundary layer. Finally the effective intermittency γ_{eff} is calculated as $\gamma_{eff} = \max(\gamma, \gamma_{sep})$. When coupled with other turbulence models, e.g. $k-\omega SST$ used in the present study, γ_{eff} controls the production term in the k equation to generate turbulence.

2.4 COMBINATION OF LAMINAR SEPARATION AND CAVITATION

To create a transition sensitive cavitation mass transfer model, a first approach could be to modify the vaporization factor C_v with the laminar separation criterion as $C_v \cdot \gamma_{sep}$. However, directly using γ_{sep} will lead to a problem that predicted cavitation will never attach to the wall surfaces leaving viscous sub-layer remaining non-cavitating. This is because using the transition model, the transition will always be triggered in the middle of the boundary layer. This is due to its fundamental formation of the criterion related to the vorticity Reynolds number $Re_v = \frac{\rho y^2}{\mu} S$ which has its maximum values in the middle of the boundary layer. Thus the γ_{sep} needs to be modified to cover the region between the predicted location around the middle of the boundary layer, and the wall surfaces including the viscous sub-layer. This can be done in many different ways; in the present study it is achieved by using γ_{sep} and the cell valued wall normal direction $\mathbf{n}$, thus using mesh information relying on local properties and suitable for parallelized computations.

To explain the procedure used, note that γ_{sep} is a cell valued scalar with lower bound of 0 and upper bound of 2, and when the local value is higher than 0 it will be activated in the k equation as a source term and start to generate turbulence locally turning the laminar boundary layer into a turbulent one. From this, a parameter *SepInd* in the range 0 - 1 will be formed that controls the mass transfer from liquid to vapor. The fist step is to set $SepInd_{org} = 1.0$ for $\gamma_{sep} > 0$ and $SepInd_{org} = 0$ otherwise, and set $SepInd = SepInd_{org}$. Further, the limiting function $F_{\theta t}$ of the LCTM is changed to the explicit criterion $F_{\theta t} > 0.95$ for non-cavitating regions for robustness. Next step is to perform an ad hoc transportation of *SepInd*. This transportation is not based on velocity, instead for the present purpose *SepInd* is transported by the normalized cell wall normal direction similarly to $-\hat{\mathbf{n}}$. In order to construct the normalized 'face flux' of *SepInd*, the face value of $\mathbf{n}_f$ is interpolated from $\mathbf{n}$, and the corresponding face valued $SepInd_f$ can be set to 1.0 for a cell with $SepInd = 1.0$ and $SepInd_f = 0$ otherwise. Thus $F_f = -\mathbf{n} \cdot \mathbf{S}_f / |\mathbf{S}_f| \cdot SepInd_f$, is calculated, where $\mathbf{S}_f$ is the face area vector and $|\mathbf{S}_f|$ is the face area magnitude. Then the Gauss theorem can be used to reconstruct new cell values of $SepInd_{i,new}$ as $SepInd_{i,new} = div(F_f) \cdot V_i$. Clearly $SepInd_{i,new}$ has a maximum value of 1.0 for the perfectly parallel adjacent cells closer to the wall and a minimum value of -1.0 for the cells further away from the

wall surfaces. Then $SepInd_{i,new}$ can be set to 1.0 for $SepInd_{i,new} > 0.2$, where the value of 0.2 here is used to exclude the possible transportation for faces nearly perpendicular to the wall surfaces around 78 degrees. Lastly the $SepInd_i$ can be updated to $SepInd_i + SepInd_{i,new}$ and the process is repeated. If we consider that $gsum(SepInd)$ represents the number of cells with $SepInd = 1.0$, $gsum(SepInd)$ will monotonically increase till a converged value of $gsum(SepInd_{final})$. Lastly, $SepInd_{final}$ is used to feed to the cavitation mass transfer model by replacing the vaporization constant C_v with $SepInd_{final} \cdot C_v$. An example of the effect of this transportation can be found in figure 5.1.

The model was firstly developed in [34] and paper B with more details in paper D. In [35], a adjusted modification with similar principles is used with improved sheet cavitation predictions and validated with several detailed experiments. Especially for one case, the unbridged approach predicted similar sheet cavitation extent for propeller tested in a facility with applied roughness and the modified approach predicted similar sheet cavitation extent for the same geometry tested in the other facility with smooth blades.

2.5 FWH ACOUSTIC ANALOGY

Noise predictions can be achieved by FWH (Ffowcs Williams - Hawkings) acoustic analogy with input from numerical simulation predictions. The FWH equation rearranges the continuity and the momentum equations into the form of an inhomogeneous wave equation and was proposed in [36] considering impermeable surfaces in motion, referred to as $S-FWH$,

$$\Box^2 p' = \frac{\partial}{\partial t}[\rho_0 v_n \delta(f)] - \frac{\partial}{\partial x_i}[p n_i \delta(f)] + \frac{\partial^2}{\partial x_i \partial x_j}[H(f) T_{ij}], \tag{2.19}$$

in which $\Box^2$ represents the D'Alembertian operator, **n** represents the unit outward normal of the surface, v_n represents the local normal velocity of the surface, p represents the local gage pressure on the surface and T_{ij} represents the Lighthill stress tensor defined as

$$T_{ij} = \rho u_i u_j - \sigma_{ij} + (p' - c^2 \rho')\delta_{ij},$$

in which δ_{ij} represents the Kronecker delta and σ_{ij} is the viscous stress tensor. With a porous data surface, referred to as $PDS-FWH$,

$$\Box^2 p' = \frac{\partial}{\partial t}[\rho_0 U_n]\delta(f) - \frac{\partial}{\partial x_i}[L_i \delta(f)] + \frac{\partial^2}{\partial x_i \partial x_j}[H(f) T_{ij}], \tag{2.20}$$

in which

$$U_n = (1 - \frac{\rho}{\rho_0}) v_n + \frac{\rho u_n}{\rho_0},$$

$$L_i = p\delta_{ij}n_j + \rho u_i(u_n - v_n).$$

In equation 2.19, the first term on right hand side represents the thickness term, and the second term represents the loading term; both terms are evaluated on the impermeable data surface $f = 0$ through the Dirac delta function $\delta(f)$. The third term, including the Heaviside function $H(f)$ and the Lighthill tensor, represent the nonlinear quadrupole term outside the surface $f = 0$. When it comes to the formation on permeable data surfaces as shown in equation 2.20, the first two terms loose their physical meaning and are instead denoted as pseudo-Thickness and pseudo-Loading terms. The sampling surface with $PDS - FWH$ is expected to enclose all non-negligible quadrupole sources and thus the volume integration outside the surface is no longer needed. Farassat formulation 1A [37, 38] of this acoustic analogy was derived for aeroacoustic rotors where the solution consists of terms consisting of both near-field terms (decay with $1/r^2$) and far-field terms (decay with $1/r$). More details can be found in the original publications, also summarised in [39], with implementation details for Star-CCM+ given in [25].

2.6 SIMULATION TOOLS

Two major packages are used in the present study, which are the open-source package OpenFOAM and commercial package Star-CCM+. In both codes the set of equations is solved in the segregated manner. In OpenFOAM, the solver `interPhaseChangeFoam` is used for two incompressible, isothermal immiscible fluids with phase-change, which use VOF (volume of fluid) phase-fraction based interface capturing. A modified code based on `interPhaseChangeFoam` implemented into OpenFOAM v1806 and v1912 is mainly used. Star-CCM+ is a complete multiphysics simulation tool and as with OpenFOAM, for the presented simulated cases the fluid is assumed to be incompressible, isothermal immiscible and VOF is used for volume fraction capturing.

The used numerical schemes are described for each presented simulations in the attached publications. As a summary, throughout the simulations performed in the thesis, regarding time derivatives the implicit second order upwind Euler scheme is used in both OpenFOAM (referred to `backward`) and Star-CCM+ (referred to as `second order`) when predictions are being collected; while the implicit backward Euler with first order accuracy (referred to `Euler` in OpenFOAM and `first order` in Star-CCM+) is used for simulation initialization after converged steady-state solutions for most cases. Concerning gradient calculation, in OpenFOAM the linear scheme is typically used for face value interpolation together with Gauss theorem while in Star-CCM+ a hybrid Gauss theorem with least square method is used with the Venkatakrishnan limiter. For the calculation of convection terms, linear upwind differencing scheme is typically used for convective flux calculation which is denoted as `linear upwind` in OpenFOAM and as `second order` in Star-CCM+. Less diffusive NVD (Normalised Variable

Diagram) schemes are also used for certain cases in OpenFOAM referred to as `limitedLinear` and in Star-CCM+ simulations with IDDES turbulence model referred to as `bounded central differencing` with bounded differencing parameter of 0.15. Besides, first order upwind scheme is used regarding the convection of volume fraction α as suggested in [31]. Regarding pressure velocity coupling, the SIMPLE algorithm is always used for steady-state simulations and transient simulations in Star-CCM+. In OpenFOAM the SIMPLE-C algorithm is used for steady-state cases and the PIMPLE algorithm is used for transient simulations. PointWise is the major package for mesh generation while Star-CCM+ built-in meshers are used if simulations are performed only in Star-CCM+.

3

Studied cases

3.1 A GENERAL CARGO VESSEL WITH LDP

The studied case here is the ship with LDP (Large Diameter Propeller) designed in the LeanShips (Low Energy And Near to zero emissions Ships) project. The extremely low tip clearance ($\sim 1\%$) makes a higher efficiency propeller system come true but clearly induced hull pressure pulse should be assessed.

Several conditions were considered in the present study summarized in Table 3.1, which are named Condition A, B1 and B2 here. The model scale experiments were carried out in the DWB (Depressurized Wave Basin) at MARIN (Maritime Research Institute Netherlands) and induced pressure pulses were recorded by 14 pressure traducers. The views of meshes are shown in figure 3.1 and the arrangement of pressure transducers are shown in figure 3.2.

There are 18.4 million cells in the model scale condition A with $y+$ ranging from 25 - 80 on the ship hull and $y+ < 1$ on the propeller blades. For the full scale condition B1 and B2 there are 22.7 million cells with $y+$ ranging from 25 to 180 on both ship hull and propeller blades.

Conditions	Scale	Free surface	Wall roughness
A	Model	no	Smooth
B1	Full	no	Smooth
B2	Full	no	Rough (120 micrometers)

Table 3.1: Summary of simulation conditions.

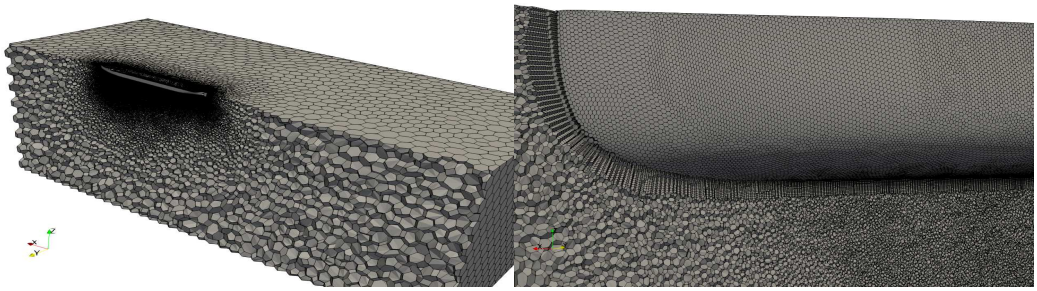

(a) Simulation domain for condition B (b) Volume mesh close to the forebody

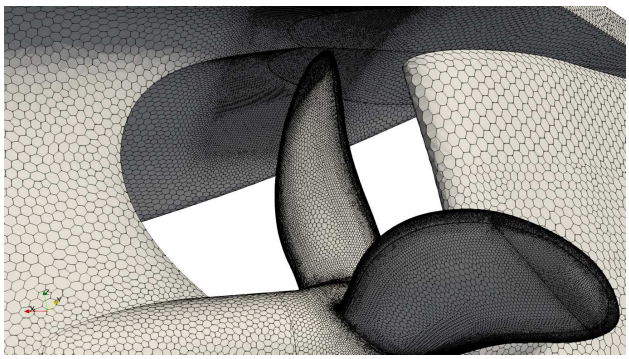

(c) Propeller and aft-body surface mesh

Figure 3.1: Views of computational grids.

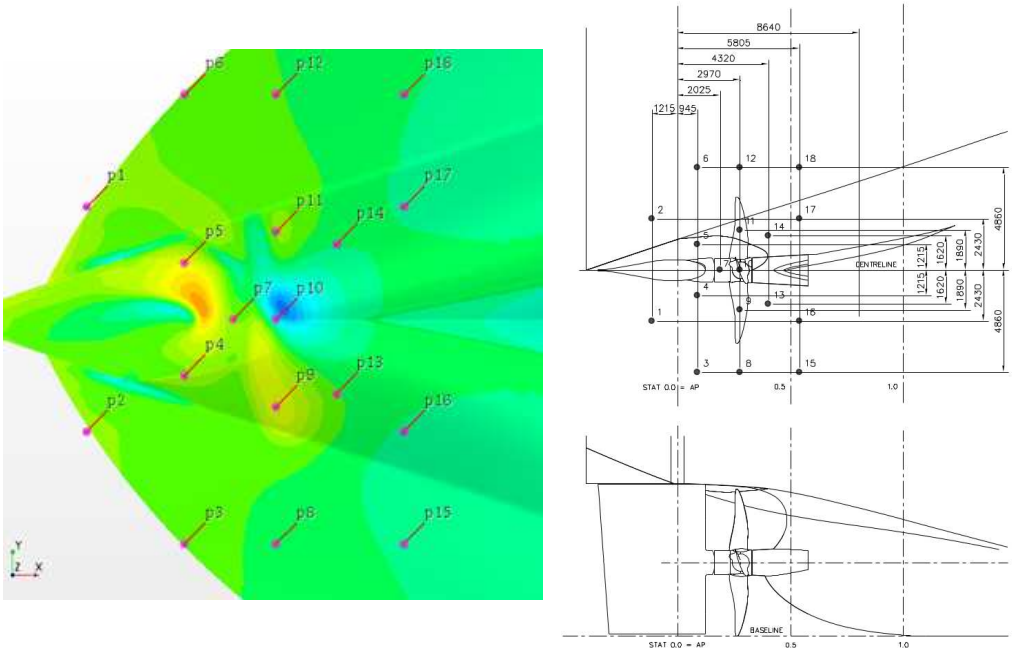

Figure 3.2: Arrangement of pressure transducers.

3.2 Open-water propellers on inclined shaft

3.2.1 Kongsberg propeller A and propeller B

Experiments were performed in the cavitation tunnel T31 at Kongsberg Hydrodynamic Research Centre in Kristinehamn, Sweden. The two studied propellers have similar designs and propulsion characteristics while one is slightly more tip unloaded than the other one. Thus the first objective is to investigate the design influence to the cavitation phenomenon and pressure pulses both experimentally and numerically. The geometries are shown in figure 3.4 including surrounding grids.

The propeller shaft was inclined about 10 degrees to create blade load variations. The propellers were tested under different advance ratios J and cavitation numbers σ. Eight pressure transducers were placed on the top wall of the cavitation tunnel test section above the propeller to measure induced pressure pulse levels. High speed videos were recorded for detailed study of related cavitation phenomenon. Experimental measurements show that only the blade harmonic frequency pressure pulses are significant and those of higher harmonics are small enough to be neglected.

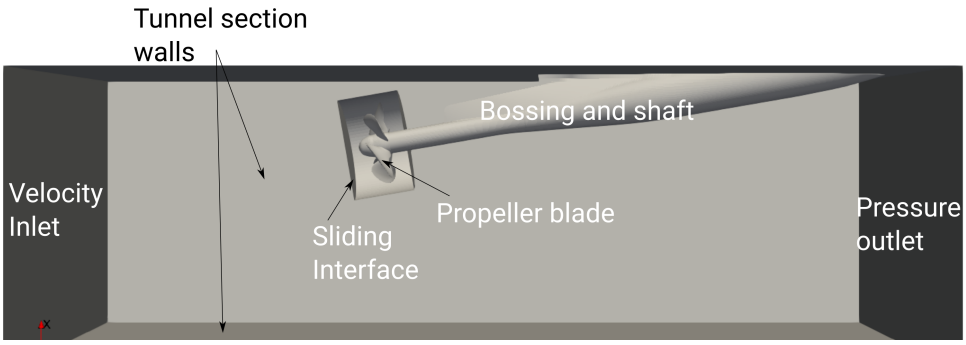

Figure 3.3: Simulation domain and boundary conditions for the Kongsberg propeller simulations.

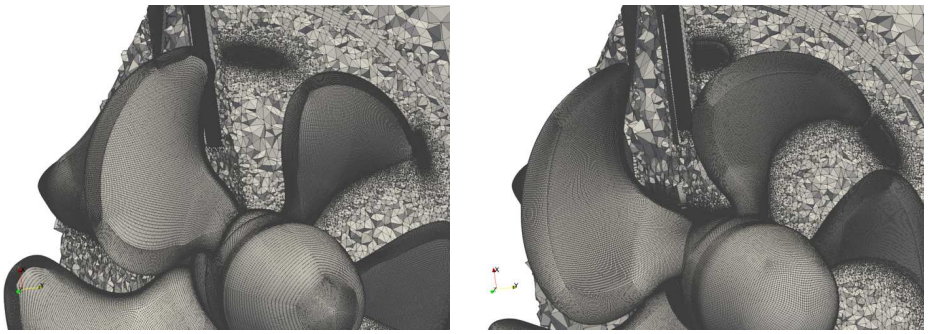

Figure 3.4: Geometry and meshes of propeller A (left) and propeller B (right).

An emerging problem is the over-predictions of massive sheet cavitation on propeller blades, which are predicted very similarly using both Star-CCM+ and OpenFOAM for all the studied meshes and studied operating conditions with different J and σ. The over-predictions lead to inaccurate numerical predictions of pressure pulses under cavitating conditions.

Comparing to high-speed videos, it was noticed that the blade regions covered by over-predicted sheet cavities in numerical simulations, were found with mostly intermittent traveling bubble cavities or developing cavity strips in the experiments. These observations were noticed on three other tested propellers which were tested under similar experimental configurations, thus no further numerical studies performed for the other propellers.

Using a transition sensitive turbulence model, it was found that the over-predicted cavities overlap with laminar-transitional boundary layer under non-cavitating conditions. Furthermore, a literature survey shows a correlation between sheet cavitation and laminar-transitional flow, thus the NACA 16012 hydrofoil was further investigated to understand the pre-mentioned issue with developing of a bridged model which bridges the transition sensitive turbulence model and cavitation mass transfer model. The bridged model is then applied to the two Kongsberg propellers with significantly improved cavitation predictions. The literature survey also revealed that the massive over-prediction of sheet cavitation is not rare, and a publicly available propeller PPTC VP1304 is studied using the ordinary approach and the bridged model as well. This propeller was studied in the first and second workshops on cavitation and propeller performance, held on the second and fourth International Symposium on Marine Propulsors [40, 22].

3.2.2 PPTC VP1304 propeller

In the second SMP workshop [22], the propeller was mounted on an inclined shaft with inclination angle of 12°. The propulsion characteristics, cavitation behavior and pressure pulses of the propeller operating in oblique flow were measured and studied by various research groups using various numerical methods, including BEM, RANS and ILES with different cavitation mass transfer models. Present study focuses on the task 2.1 in the original workshop, which is a cavitating case with advance ratio $J = 1.019$ and cavitation number $\sigma = 2.024$, summarized in table 3.2. This corresponds to very representative configurations for marine propeller cavitation experiments, i.e. propeller mounted on inclined shaft to create propeller inflow variations and thus cavitation dynamics. In the original workshop, the majority of participants reported similar cavitation patterns with massively over-prediction on certain blade locations compared with experimental recordings, with the common simulation approaches using different mesh resolutions and mesh types, flow solvers, turbulence models and cavitation mass transfer models. Thus the case can be an interesting validation case to investigate the sheet cavitation over-prediction phenomenon. The main characteristics of VP1304 is summarized in table 3.3, with numerical configurations shown in figure 3.5.

Advance ratio J	Cavitation number σ	Rotation speed
1.019	2.024	20 rps
Water density ρ_l	**Water kinematic viscosity ν_l**	**Vapor pressure**
997.78 kg/m^3	$9.567 \cdot 10^{-7}$ m^2/s	2643 Pa

Table 3.2: Studied operating condition of VP1304.

Diameter	Pitch	Chord length(0.7R)	Pitch ratio(0.7R)	Skew	Blades no.
250 mm	408.75 mm	104.167 mm	1.635	18.8°	5

Table 3.3: Main characteristics of propeller VP1304.

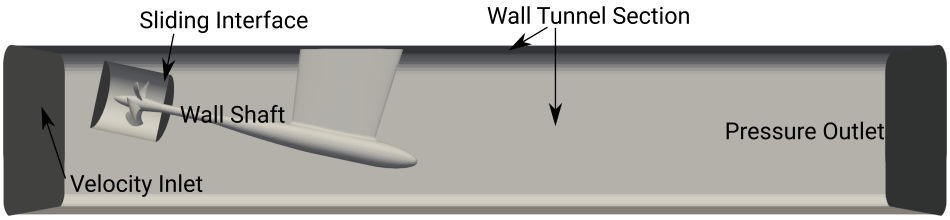

Figure 3.5: Simulation domain and boundary conditions, VP1304 case 2.1.

The computational mesh was generated using Pointwise. Structure-meshed surfaces and hyperbolic extrusion of conformal prism cells are used and fulfill the requirements of the transition model usage, and tetrahedral cells are used to fill the rest simulation domain. General views of surface and volume mesh are shown in figure 3.6 close to the leading edge at the blade tip. There are 27 million cells in the propeller rotation region and 2 million cells for the test section.

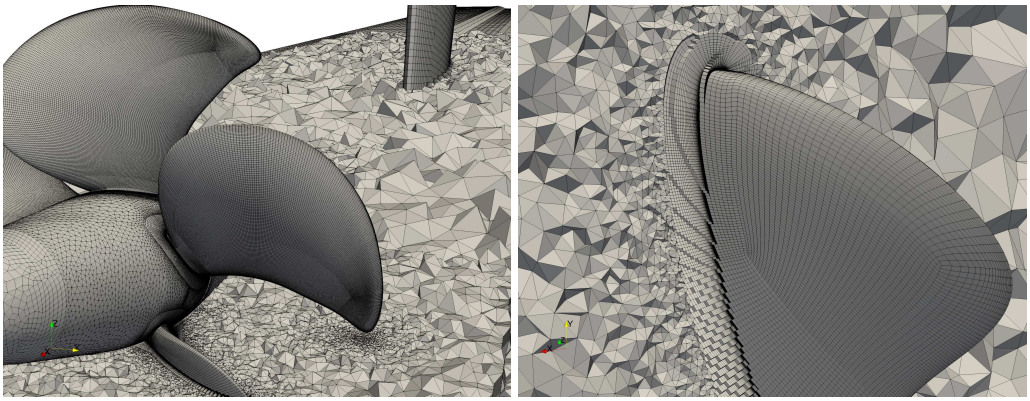

Figure 3.6: Closer grid view at blade edge.

3.3 NACA16012 HYDROFOIL

The NACA16012 hydrofoil, especially the condition under AoA of 3°, clearly reveals the relationship between laminar separation and sheet cavitation inception as discussed in [41, 42]. As a case to understand the relationships between sheet cavitation and predicted separation, as well as a case to develop a usable model, the NACA16012 hydrofoil is studied. The experiments were performed in Grenoble University and experimental results have been published in details in [41]. The hydrofoil was tested in a free-surface channel with different angles of attack, cavitation numbers and Reynolds numbers. One of the advantage of this study case is that the free-stream turbulence rate is reported, which is known to be important for transition prediction and required by the usage of the $\gamma - Re_\theta$ transition model.

The hydrofoil was mounted inside the test section with main dimensions of 1.6 m × 0.12 m × 0.4 m (L × W × H) with a submersion depth of 0.2 m. The foil chord length c is 0.1 m and its maximum thickness at the relative abscissa 0.5 is 1.2 cm. Colored water was injected close to the leading edge to visualize the boundary layer separation. Under different test conditions, the velocity varies from 3-12 m/s and the turbulence rate Tu varies from $0.12\% - 0.16\%$. The simulations include AoA of 0°, 3°, 4° and 5°, with focus on the discussion with AoA of 0° and 5° for both cavitating and non-cavitating conditions, as shown in table 3.4.

Reynolds number	Cavitation number σ	Turbulence rate Tu
300,000	Non-cavitating	$Tu = 0.12\%$
1,000,000	$\sigma = 0.045$	$Tu = 0.15\%$

Table 3.4: Studied conditions of the NACA 16012 foil.

The computational mesh is shown in figure 3.7 and generated using Pointwise. A circular region close to the foil is meshed with structured grids and connected with the outer region with unstructured grids. The first cell height on the foil was calculated based on $y+ \sim 1$ with inlet velocity of 10.04 m/s, and 60 prism layers with constant growth ratio of 1.05 was generated to fulfill the requirements by the transition model. The 2D mesh consists of 0.174 million cells in total, and for the 3D simulations the 2D mesh was uniformly transformed for 30 layers in the span-wise direction with total width of 5 cm (half compared to the experimental usage), resulting in 4.86 million cells. The top free-surface was substituted with slip wall condition and the wall effects of the test section are neglected with slip boundary condition as well.

The inlet velocities U with Reynolds numbers of $300,000$ and $1,000,000$ can be calculated to be 3.012 m/s and 10.04 m/s respectively and fixed at the velocity inlet. The kinetic energy k, turbulent dissipation rate ω and turbulent viscosity ν_t at the inlet boundary are estimated via equations 3.1 with fixed viscosity ratio $R_T = 10$. Turbulence decay control is used in the simulations. The used values of

k and ω at the inlet boundary under different conditions are summarized in table 3.5.

$$Tu = 100\frac{\sqrt{2k/3}}{U}, \quad R_T = \frac{\rho k}{\mu\omega}. \tag{3.1}$$

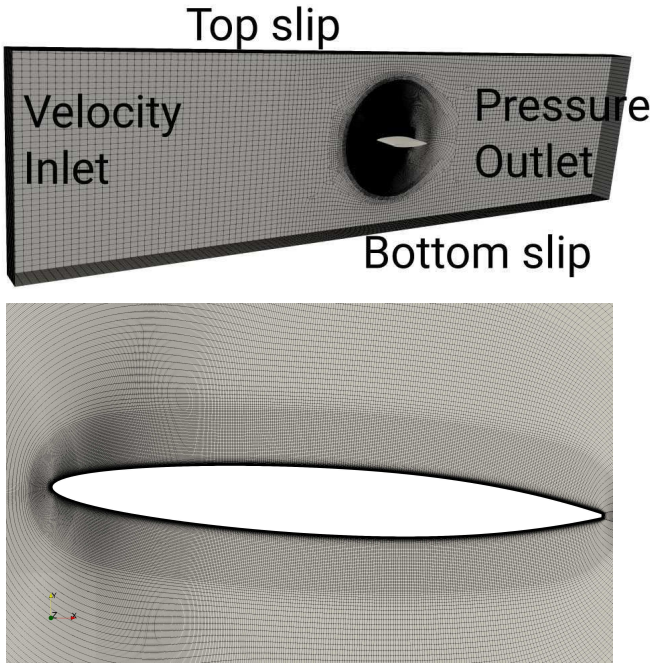

Figure 3.7: Simulation domain (upper) and closer view of computational grids (lower).

Reynolds number	U	k	ω	ν_t	$Re_{\theta t}$
300,000	3.012	1.96×10^{-5}	1.952	1.004×10^{-5}	1118
1,000,000	10.04	0.00034	33.885	1.004×10^{-5}	1094.8

Table 3.5: Inlet boundary values of the NACA 16012 foil.

3.4 A CONVENTIONAL CONTAINER VESSEL

The studied vessel is a representative design for container vessels with 3600 TEU standards, used in the VIRTUE and SONIC EU projects. Experimental studies including hull pressure pulse measurements, acoustic measurements and cavitation pattern observations, were preformed at HSVA in the largest cavitation tunnel HYKAT. The model scale ship hull was mounted inside the large size cavitation

tunnel and the model scale propeller was tested operating inside the ship wake, resulting a relatively complete and representative test case. The container vessel is equipped with a single fixed pitch five-bladed propeller with high-skewed blades and the main geometry characteristics of the full scale vessel and the paired propeller are summarized in table 3.6.

	Full scale ship data
Length between perpendiculars, Lpp	232.0 m
Beam, moulded	32.2 m
Draft at forward/aft perpendiculars	11.3 m
Displacement	50885.0 m^3
Block coefficient, CB	0.602
Waterplane coefficient, CW	0.809
Propeller distance from aft perpendicular	4.8 m
Number of propellers, NP	1
Propeller Diameter, D	7.9 m
Rotation	Right handed
Pitch ratio P0.7R/D	1.109
Chord length at 0.7R	2.5 m
Propeller tip clearance	27.7 %D

Table 3.6: Main geometry characteristics of the container vessel and paired propeller.

In the experiments the propeller rotation speed was fixed to 28 rps, which is similar to typical propeller open-water test and higher than required by the Froude's law of scaling. The resulting blade Reynolds number is about 1.52×10^6. The inlet velocity was adjusted to match with desired non-dimensional thrust coefficient K_T and the pressure was adjusted to the required cavitation number σ at 0.8 blade radius located at 12 o'clock position.

Hull pressure pulses were measured via 13 pressure transducers mounted on the ship hull above the propeller. The arrangement of the transducers are shown in the left frame in figure 3.8. The transducers were of the strain gauge type (Kulite XTM 190) with suitable frequency range up to 50 kHz. A low pass filter was used for the amplifier and the resulting frequency range was limited to maximum of 1 kHz and the first to fifth harmonics pressure pulses were reported at spectrum tonal values.

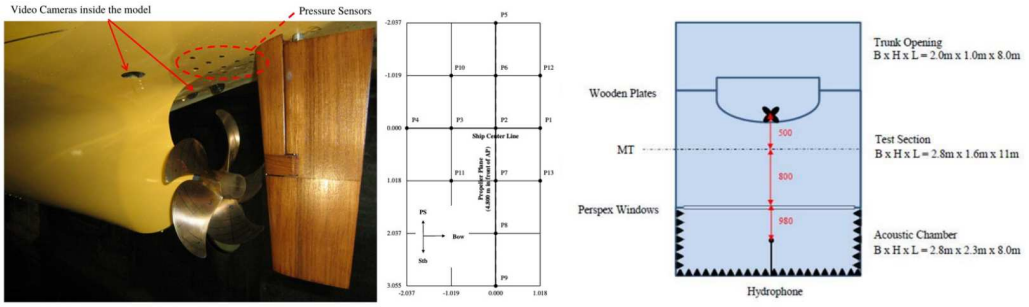

Figure 3.8: Pressure transducers and acoustic hydrophone arrangements in the experiments.

For the hydroacoustic measurement, an omnidirectional hydrophone was placed inside an anechoic acoustic chamber connected to the test section via perspex windows, as demonstrated in the right frame of figure 3.8. The acoustic signals at the hydrophone were recorded and converted into power spectrum and stored by a commercial dual channel FFT analyser. The transmission loss (TL) in the tunnel HYKAT was measured via a well-defined omnidirectional transmitter with sine sweep signal.

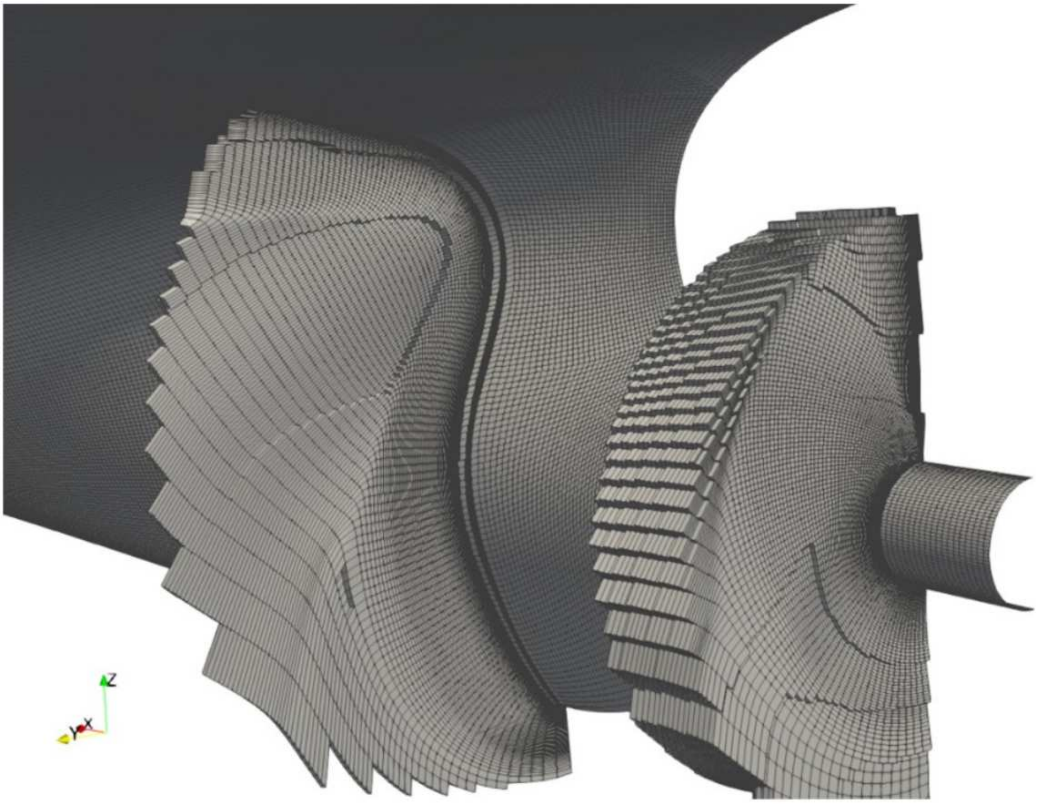

Figure 3.9: Benchmark mesh used for wake study.

The wake study was performed with meshes generated by Star-CCM+ built-in polyhedral mesher as well as a benchmark mesh generated in Pointwise shown in figure 3.9; more details can be found in paper A. There are two sets of meshes used for further study with the operating propeller. The fist set of meshes were generated using Pointwise and used in paper A, focused on the hull pressure pulse predictions under two Reynolds numbers by different scaling laws, tip region refinements and cross comparison between Star-CCM+ and OpenFOAM predictions using the RANS approach. The ship region mesh is similar to the benchmark mesh used for wake study shown in figure 3.9 and the propeller mesh, referred to as base mesh and tip refined mesh for the mesh without/with tip region refinements, shown in figure 3.10. There are in total 34.2 million cells in the base mesh and 40 million cells in the tip refined mesh, with $y+ < 1$ on both ship hull and propeller blades.

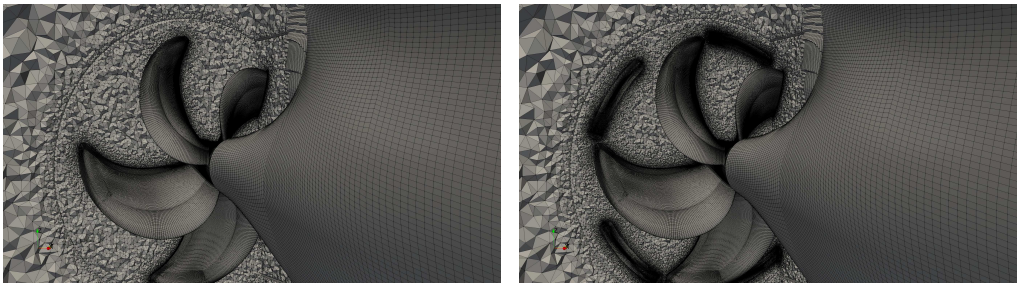

Figure 3.10: Base mesh and tip refined mesh.

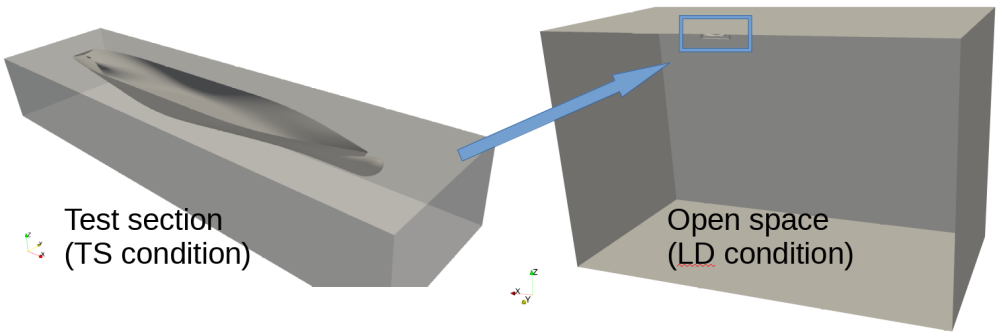

Figure 3.11: Simulation domain for TS condition (left) and LD condition (right).

The second set of meshes, generated using Star-CCM+ built-in polyhedral mesher, consists of a TS condition mesh and a LD condition mesh as shown in figure 3.11, for hull pressure pulse predictions and noise predictions using the IDDES approach. The TS condition refers to simulations with a computational domain identical to the test section and the LD condition refers to simulations with a very large computational domain. The volume mesh close to the aft-body

is shown in figure 3.12 and closer view of propeller blade mesh is shown in figure 3.13.

It can be noted, as shown in figure 3.12, that there are two pre-defined PDS, denoted $PDS-L1$ and $PDS-L2$, which are used as input surfaces for the FWH acoustic analogy. $PDS-L1$ encloses the propeller, rudder and the downstream wake; $PDS-L2$ encloses the whole ship-propeller configuration as a large rectangular box. More details can be found paper E.

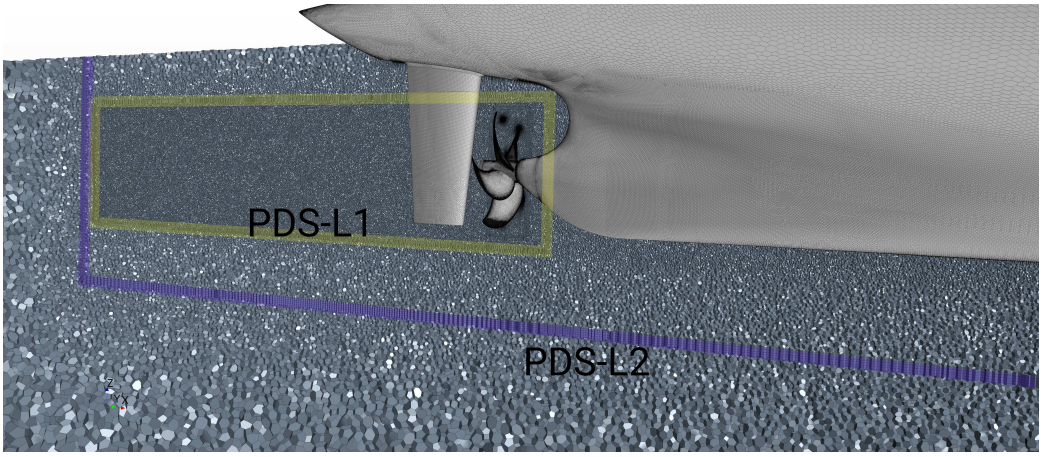

Figure 3.12: Volume mesh close to the aftbody and placements of *PDS*.

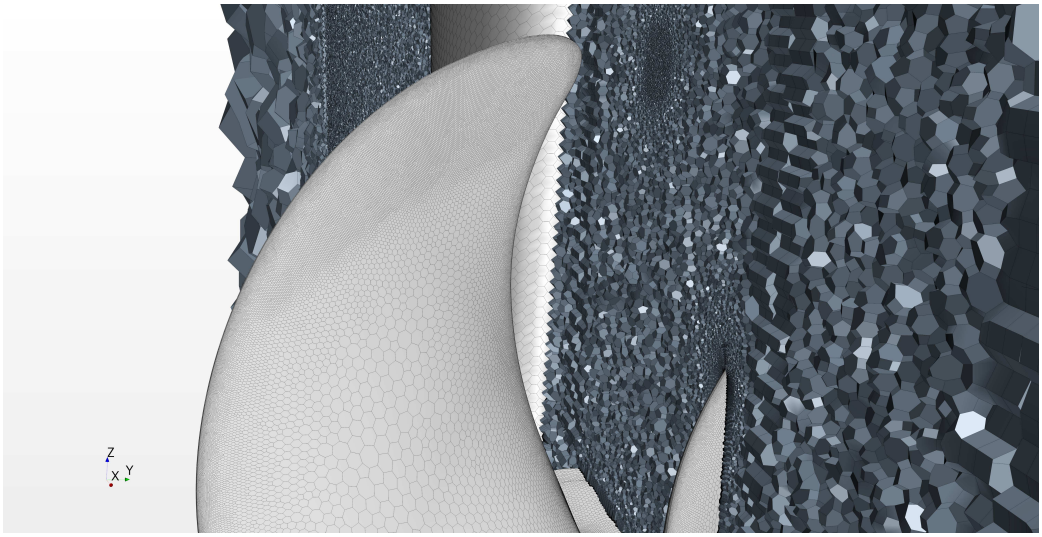

Figure 3.13: Surface and volume mesh close to propeller blades.

4

Non-cavitating condition pressure pulses

For the two studied Kongsberg propellers, the predicted non-cavitating pressure pulses generally agreed well for all the transducer locations with slight under-predictions, as summarized in figure 4.1 for both propellers with different operating conditions, and provided satisfying comparative study between the two similar propeller designs. More details can be found in paper B.

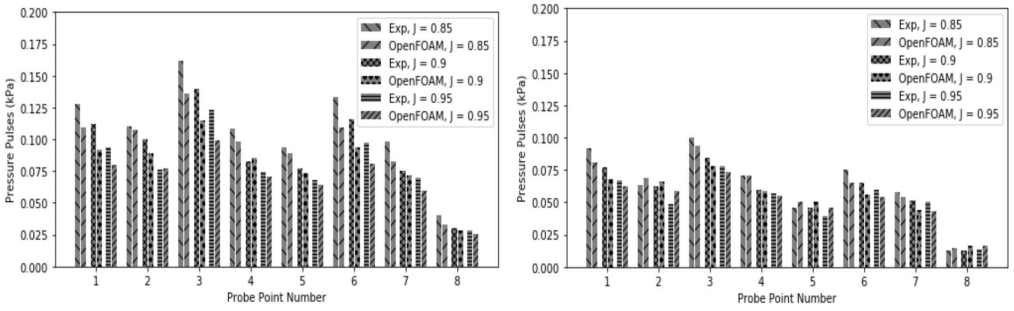

Figure 4.1: Predicted BPF pressure pulses for propeller A (left) and propeller B (right).

The predictions with different meshes for the Kongsberg propeller A are summarized in figure 4.3, with meshes consist of cell counts ranging from 7.2 million to 26.3 million, shown in figure 4.2. With the usage of the $k-\omega$ *SST* and $\gamma-Re_\theta$ transition turbulence model, up to $4\% \sim 5\%$ difference of K_T were predicted while no clear prediction differences of pressure pulse levels can be found, shown in the right frame in figure 4.3.

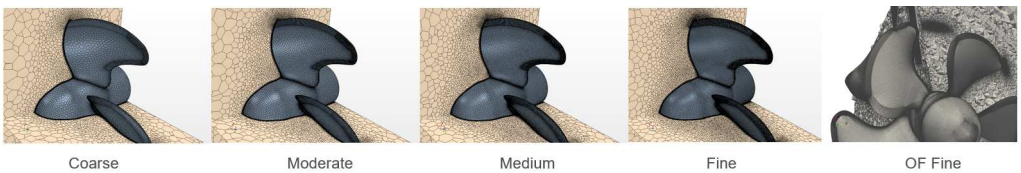

Figure 4.2: Different meshes used for propeller A.

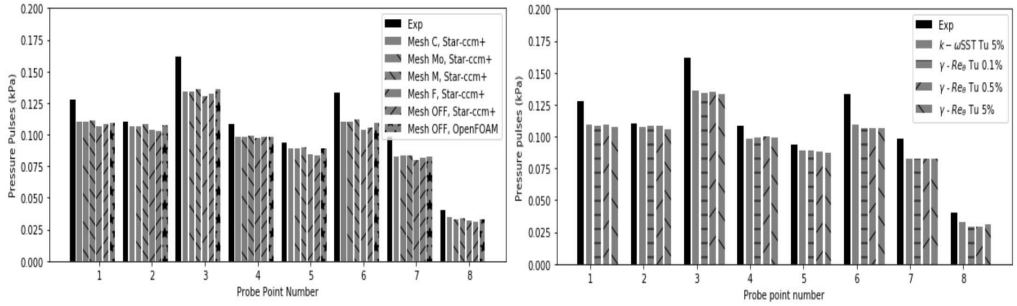

Figure 4.3: Predicted BPF pressure pulses for propeller A using different meshes and packages (left) and turbulence treatments (right).

For the container vessel, the non-cavitating hull pressure pulses are shown in figure 4.4. All the numerical predictions are consistent despite the fact of different scaled Reynolds numbers, used simulation packages and resolved tip vortex flows as details shown in paper A. The BPF pressure pulses are dominating as well.

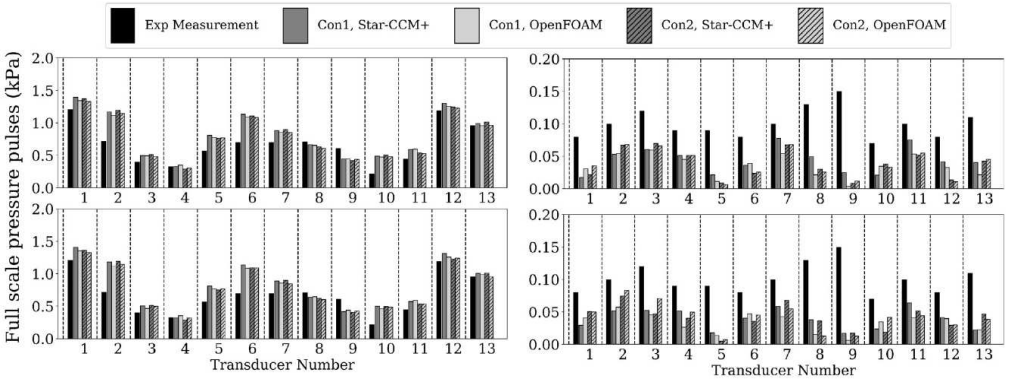

Figure 4.4: Predicted BPF (left column) and second harmonics of BPF (right column) pressure pulse levels using tip refined mesh (upper row) and base mesh (lower row).

As a unique design, the cargo ship with LDP shows the importance of propeller tip clearance and resulting significant non-cavitating pressure pulses rich in high frequencies. The predictions and model scale measurements are shown in figure 4.5 for simulation condition A, B1 and B2, referring to model scale simulation, full scale simulation and full scale simulation with roughness.

The pressure pulses levels are very high. The pressure pulse PSDs at transducer No.10 are shown in figure 4.6 comparing model scale simulations and measurements. The signal is rich in very high frequencies and agree well between numerical predictions and experimental measurements. The time history of recorded pressure fluctuations are shown in figure 4.7. The pressure history shows that the propeller blade suction side is responsible for the high levels of pressure pulses. The transient passage of each propeller blade lead to pressure fluctuation that contain very sharp peaks and resulted similarly in a signal with repeated unit impulses,

which lead to high frequency components in the spectral domain.

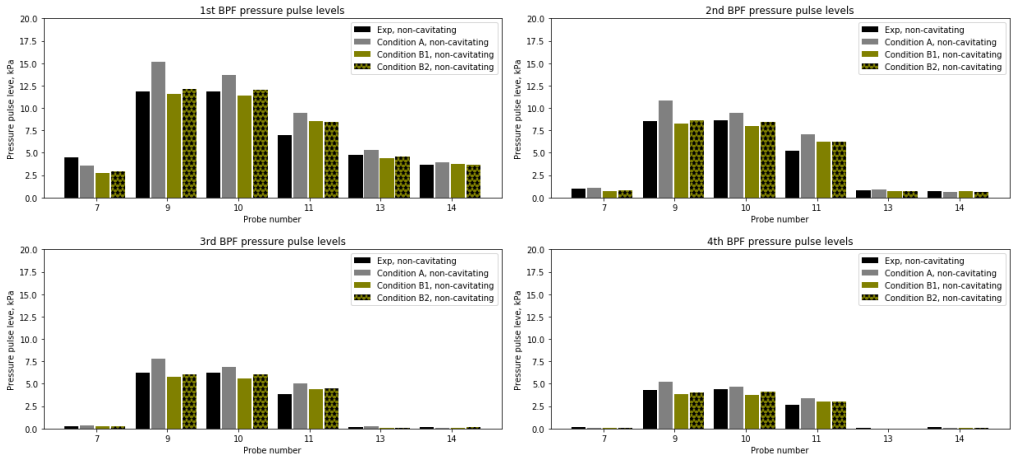

Figure 4.5: Pressure pulse levels at selected locations, non-cavitating condition.

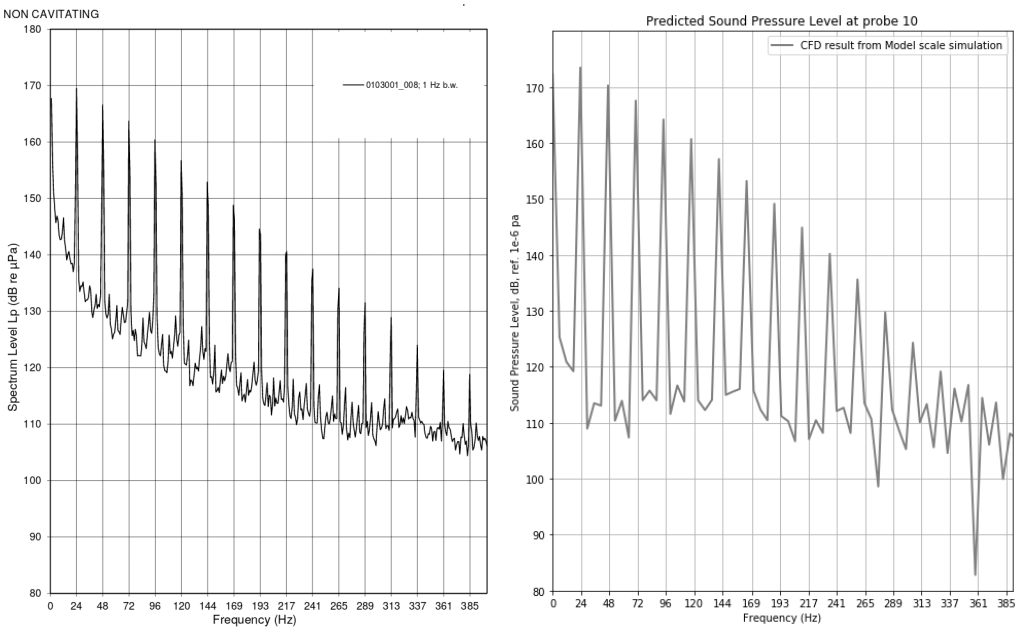

(a) Experimental measurement

(b) CFD model scale prediction

Figure 4.6: Comparison of sound pressure level at probe 10.

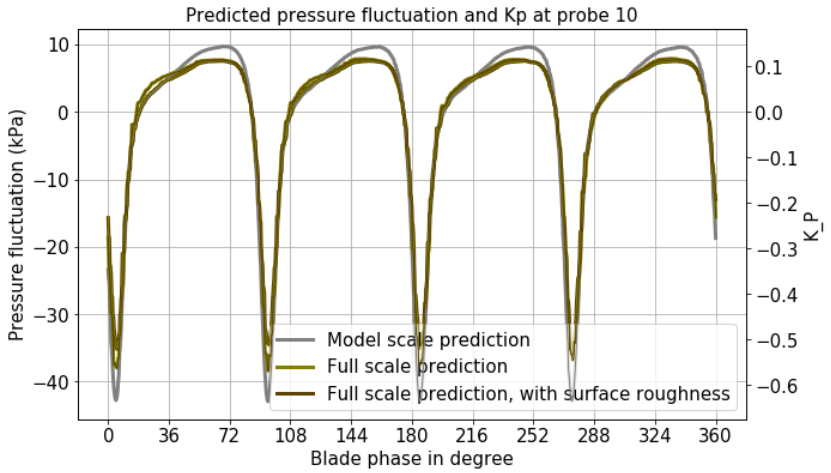

Figure 4.7: Predicted pressure fluctuation and K_p at probe No. 10.

The relative hull pressure pulse levels between the studied conditions can be related to the wake or the propeller axial inflow, as shown in figure 4.8. The propeller axial inflow is relatively compressed in the full scale configuration (condition B1) comparing to the model scale configuration (condition A) and the full scale configuration with hull roughness (condition B2), due to the boundary layer thickness difference with different Reynolds numbers or roughness effect.

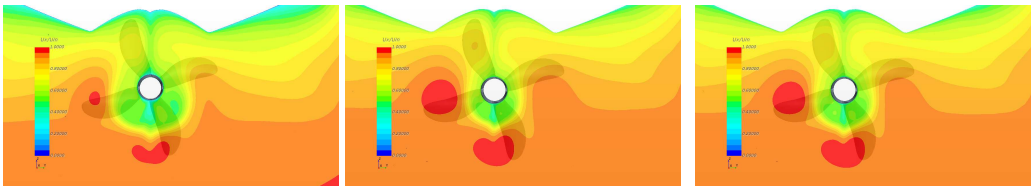

(a) Condition A (b) Condition B1 (c) Condition B2

Figure 4.8: Propeller inflow at blade phase of 22.5 degrees under different conditions

5

Sheet cavitation inception

5.1 NACA 16012 HYDROFOIL

2D non-cavitating simulations are presented first to check the accuracy for the prediction of separation location. The locations of numerical predicted separation are reported based on the cell center location where the $\gamma_{sep} > 0$ is satisfied, which is also the same location where $SepInd = 1$ is satisfied. The measured and predicted locations of laminar separation are summarized in table 5.1. In table 5.1, the experimental locations are reported based on the photos in the original paper[41]. The visualization of laminar separation, numerical predicted *SepInd* and velocity on flow direction are shown in figure 5.1 for AoA of 5° as an example.

AoA	Laminar Separation Location (EXP)	Laminar Separation Location (CFD)
0°	74 $\sim$ 80 % c	80 % c
3°	73 $\sim$ 77 % c	74 % c
4°	40 $\sim$ 60 % c	67 % c
5°	3 $\sim$ 5 % c	3 $\sim$ 6% c

Table 5.1: Predicted laminar separation location and comparison to experimental photo, Re = 300,000.

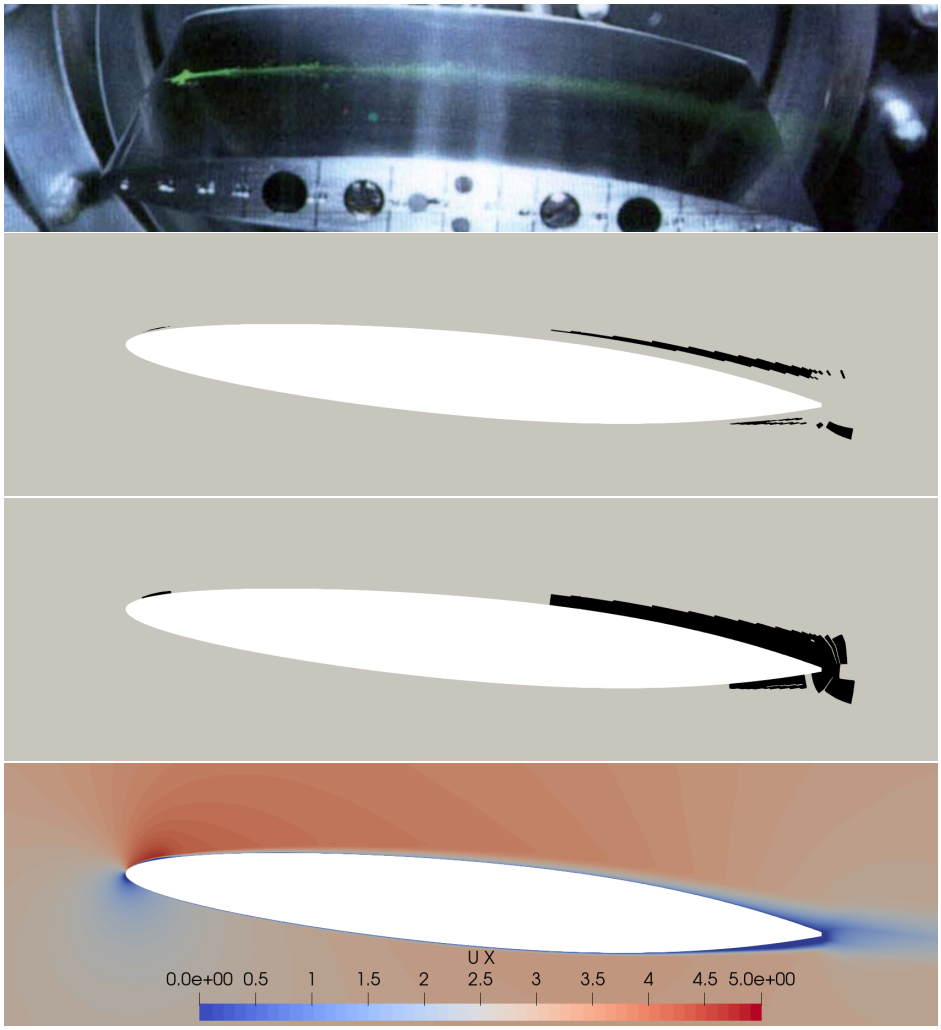

Figure 5.1: Visualization of laminar transition for NACA16012, AoA = 5°, Re = 300,000. From top to bottom: Experimental photography; predicted $SepInd_{org}$; predicted $SepInd$; predicted velocity on flow direction.

For cavitating conditions, the experimental photo, numerically predicted cavitation patterns using the bridged model and ordinary model with $k-\omega$ SST and $\gamma - Re_\theta$ are presented for AoA with 0° and 5°. The bridged model predicted significantly improved cavitation patterns and agree rather well comparing to experimental observations. The predicted sheet cavitation inception locations are summarized in table 5.2. More details and discussions can be found in paper D.

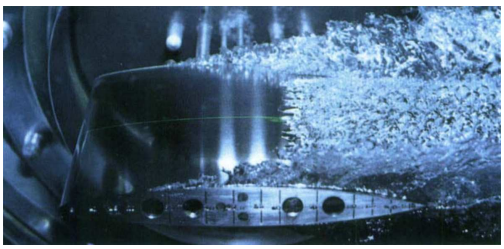

(a) 0°, EXP

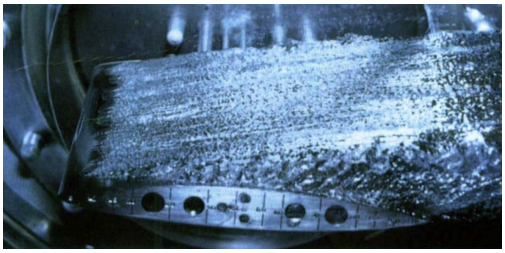

(b) 5°, EXP

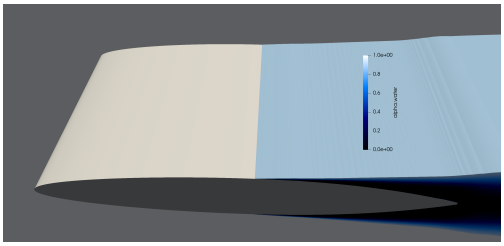

(c) 0°, bridged model, 3D

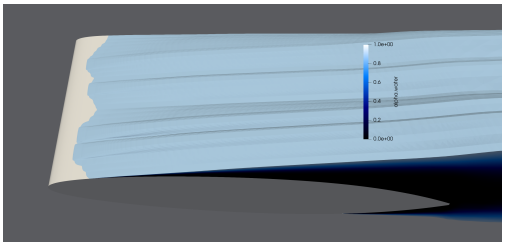

(d) 5°, bridged model, 3D

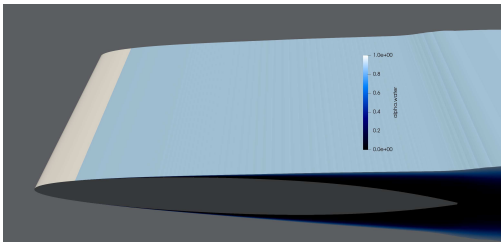

(e) 0°, unbridged $k-\omega$ $SST+SS$, 3D

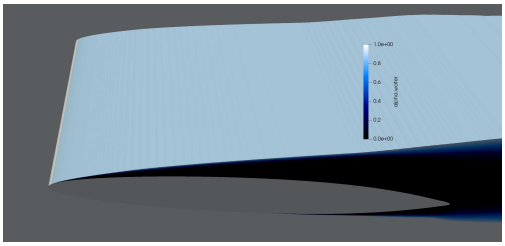

(f) 5°, unbridged $k-\omega$ $SST+SS$, 3D

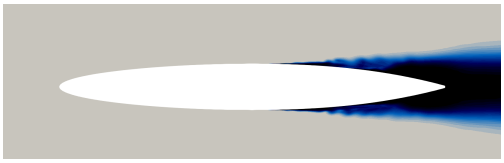

(g) 0°, bridged model, 2D

(h) 5°, bridged model, 2D

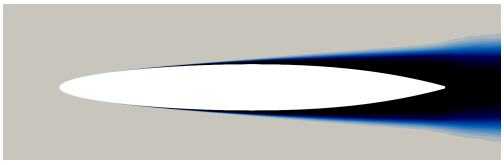

(i) 0°, unbridged $\gamma-Re_\theta+SS$, 2D

(j) 5°, unbridged $\gamma-Re_\theta+SS$, 2D

Figure 5.2: Cavitation patterns on NACA 16012 at AoA of 3° and 5°. Re = 1,000,000; σ = 0.045.

AoA	Exp	Bridged model	$k-\omega\ SST+SS$
0° (2D)	60% c	60.1 % c	11% c
0° (3D)	60% c	59 % c	11% c
3° (2D)	29% - 45% c	32% c	0.1%
4° (2D)	13% - 23% c	20.5% c	0.1%
5° (2D)	6% - 7% c	8.7% c	0.1%
5° (3D)	6% - 7% c	5 - 8% c	0.1%

Table 5.2: Summary of sheet cavitation inception locations.

5.2 VP1304 MOUNTED ON INCLINED SHAFT

Predictions under non-cavitating condition are presented first and the predictions are shown in figure 5.3 using the $\gamma-Re_\theta$ transition model and $k-\omega\ SST$ turbulence model in figure 5.4. The Q-criterion with iso-surfaces of 3×10^5 are shown contoured by pressure, and the pressure legend lower limit is set to saturation pressure. Besides, the skin friction is also shown on the propeller blades with wall limiting stream lines, with predicted *SepInd* shown in black regions on the blade surfaces. The transition model predicted strip like structures as well as *SepInd* on the leading edge at blade outer radii and strip like structures on the blade suction side. The propulsion characteristics under non-cavitaing condition are summarized in table 5.3; higher thrust coefficient K_T is predicted using the transition model, which is commonly noticed with propellers operating under relatively higher J, and can be possibly improved by using a cross-flow correlation which is not included in the present study.

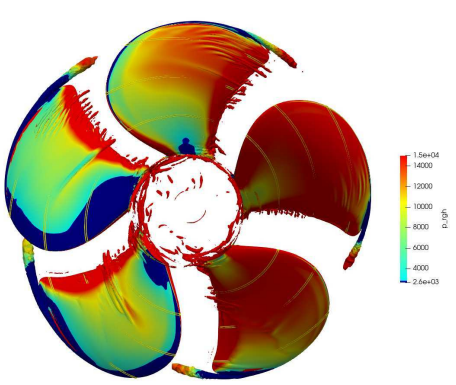

(a) Q = 3×10^5 contoured by pressure

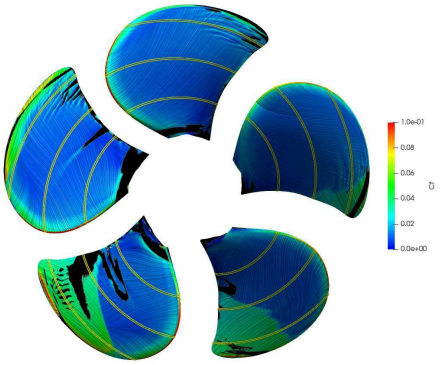

(b) *SepInd* with wall limiting streamlines contoured by C_f

Figure 5.3: PPTC VP1304 mounted on 12° inclined shaft, J = 1.019, non-cavitating condition predictions using $\gamma-Re_\theta$ model with calculated *SepInd*.

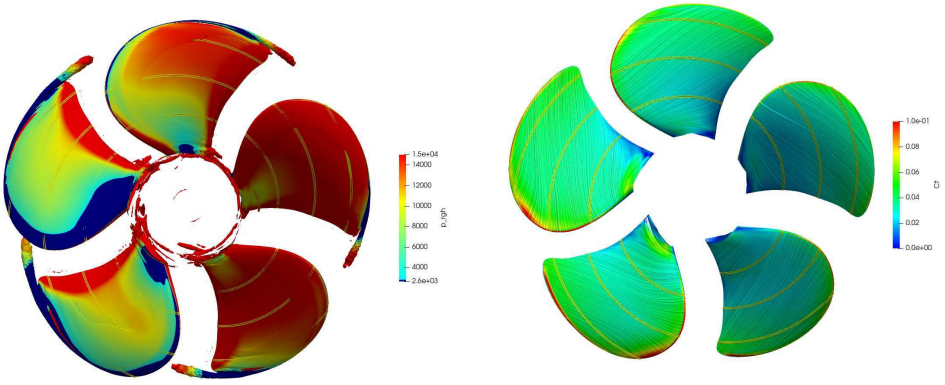

(a) Q = 3×10^5 contoured by pressure

(b) Wall limiting streamlines contoured by C_f

Figure 5.4: PPTC VP1304 mounted on 12° inclined shaft, J = 1.019, non-cavitating condition predictions using $k-\omega$ *SST* model.

$J = 1.019$	Cavitation number σ	K_T	$10K_Q$
EXP	non-cavitating	0.392	1.010
$\gamma - Re_\theta$	non-cavitating	0.408	1.010
$k-\omega$ *SST*	non-cavitating	0.393	0.990

Table 5.3: Predicted non-cavitating propulsion characteristics.

The predicted cavitation patterns using the bridged model are shown in the upper frames in figure 5.5 and predictions using the $k-\omega$ *SST* turbulence model and Schnerr-Sauer mass transfer model are shown in the lower frames. The unbridged predictions are very similar with most predictions by different institutes participated and published in the 2^{nd} SMP workshop using different FVM approaches. The bridged model predicted significantly improved cavitation pattern including the small strip-like cavity structure around mid-radius. Some discrepancies can be found regarding predicted propulsion characteristics shown in table 5.4, partly due to the inherited over-predictions under non-cavitating condition using the transition model. Besides, the larger extent of sheet cavitation observed in experimental observations on the lower right hand side blade indicates there can be discrepancies between numerical settings and experimental configurations. The intense traveling bubble cavitation can not be predicted using the present approach which might also contribute to the force prediction differences. In the workshop the force predictions can be found spreading. More details and discussions can be found in paper D.

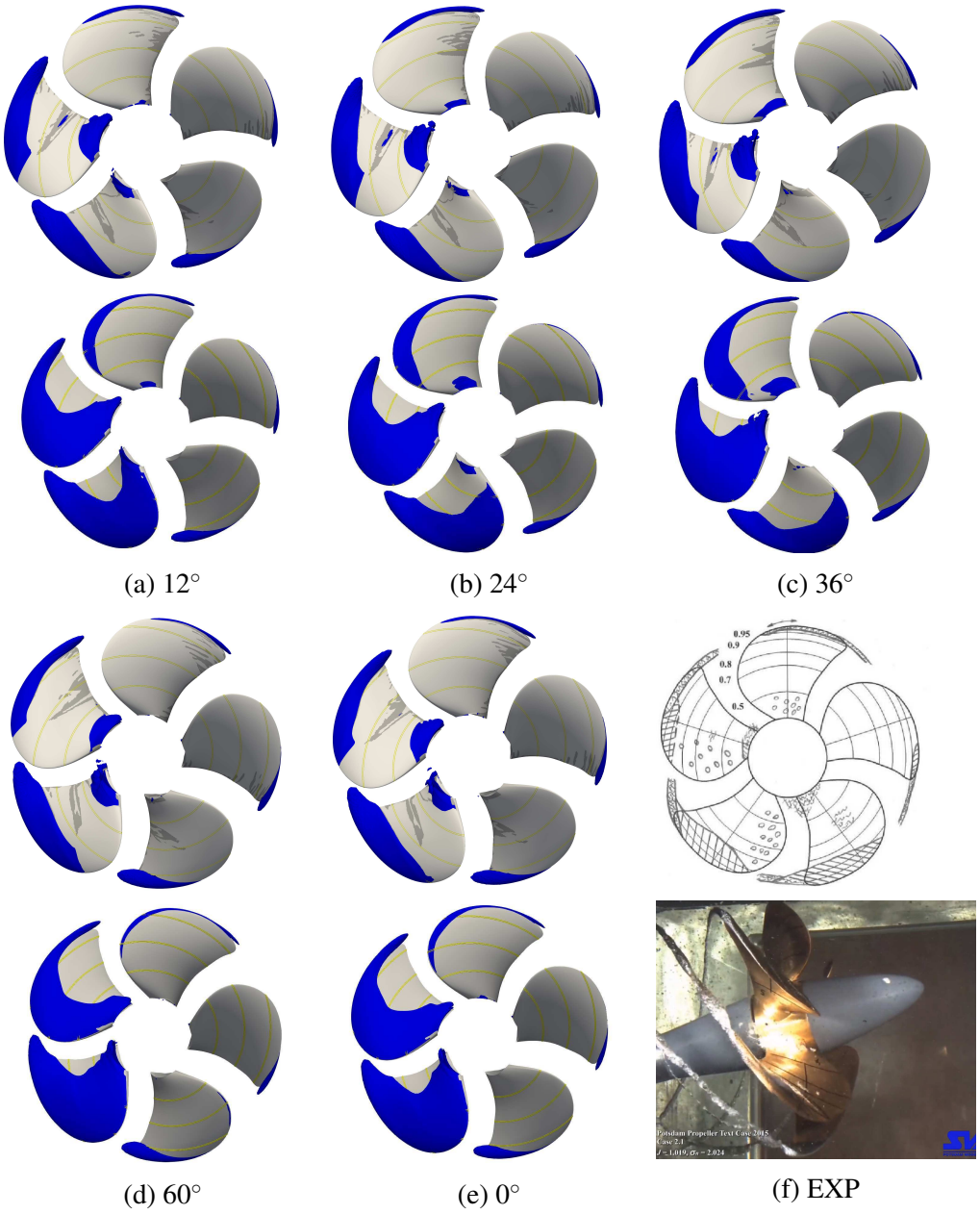

(a) 12° (b) 24° (c) 36°

(d) 60° (e) 0° (f) EXP

Figure 5.5: Predicted cavitation pattern ($\alpha_v = 0.5$) using bridged model (upper frames) and $k-\omega$ *SST* turbulence model with Schneer-Sauer cavitation model (lower frames), compared to the experimental sketch and photo snapshot.

$J = 1.019$	Cavitation number σ	K_T	$10K_Q$	ΔK_T
EXP	2.024	0.363	0.960	0.029
Bridged model	2.024	0.392	0.982	0.016
$k-\omega$ $SST+SS$	2.024	0.375	0.973	0.018

Table 5.4: Predicted cavitating propulsion characteristics.

5.3 KONGSBERG PROPELLER A

As an application case of the bridged model, the prediction results of Kongsberg propeller A is shown. Predicted *SepInd* under varying Tu are summarized in figure 5.6 under non-cavitating operating condition. The $\gamma - Re_\theta$ transition model is sensitive to the free-stream Tu; with high free-stream Tu smaller laminar-transitional boundary layer will be predicted and resulting predictions similar to the coupled $k-\omega$ SST turbulence model.

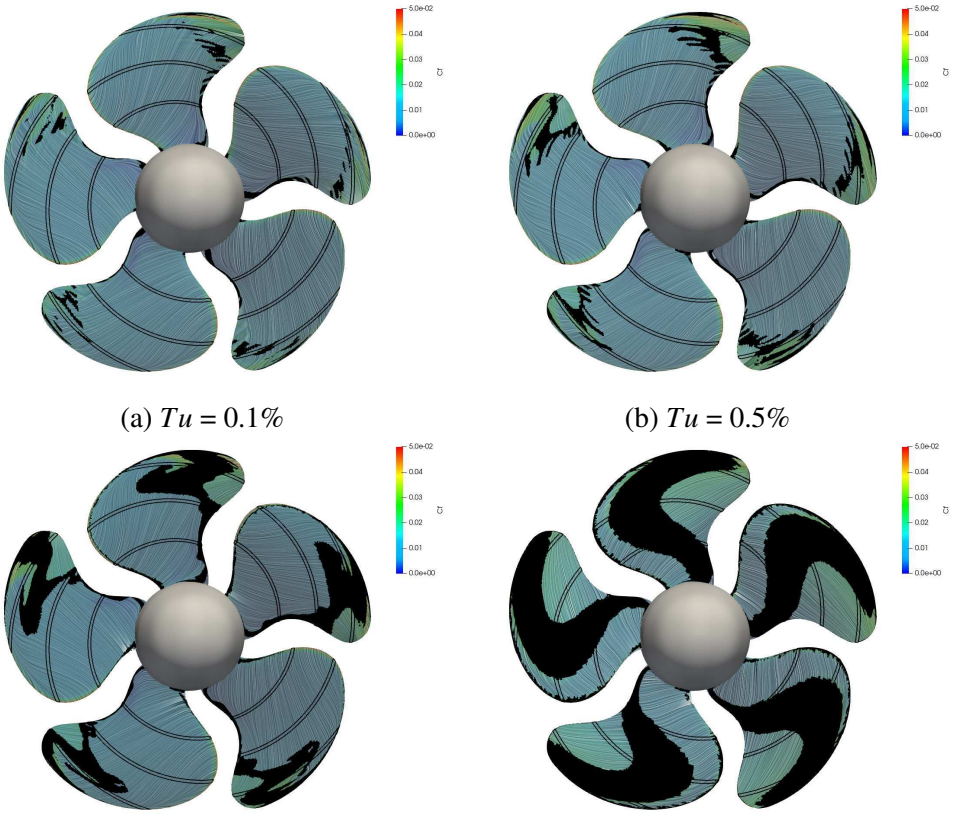

(a) $Tu = 0.1\%$ (b) $Tu = 0.5\%$

(c) $Tu = 1\%$ (d) $Tu = 3\%$

Figure 5.6: Predicted *SepInd* with different Tu.

For cavitating condition, the study focuses on the condition with $J = 0.85$ and $\sigma = 2.0$ with assumed free stream intensity level $Tu = 0.5\%$. Three typical snapshots taken by the high speed video in the experiments are shown in figure 5.7. The cavitation patterns are varying between different blade passings, but no significant difference was found between each blades, thus the variation is not suspected to be dependent on blade manufacture deficiencies nor pitch setting inaccuracies. Traveling bubble cavitation can be found on the propeller blades in the second and third frames, indicating local pressure around mid blade suction side is below saturation pressure. These traveling bubble cavitation can not attach to the blade surface but are transported downstream by the flow, with possible violent growth and collapse shown in the third frame as an example. The sheet cavitation, typically starts developing from the leading edge at around 0.95R, with some strip cavities starting from 0.9R mid-chord and develops to about 0.8R at the trailing edge. Tip vortex cavitation and limited root cavitation and root traveling bubble cavitation can be found for the present condition as well.

The predicted cavitation patterns using the unbridged approach ($k-\omega\ SST+SS$) and the bridged model ($\gamma-Re_\theta+SS+SepInd$) are shown in figure 5.8. It can be seen clearly that the sheet cavitation is massively over-predicted using the unbridged approach. For the unbridged model, the massive sheet cavitation will have significant influence on the forming of the leading edge vortex and tip vortex cavitation, which can be potentially improved by the bridged model; but in the present model the $\gamma-Re_\theta$ and the corresponding bridging is only effective inside boundary layer without predicting tip vortex cavitation. Further development is needed to make the laminar cavitation suppression active only in the boundary layer and allow for cavitation to appear elsewhere.

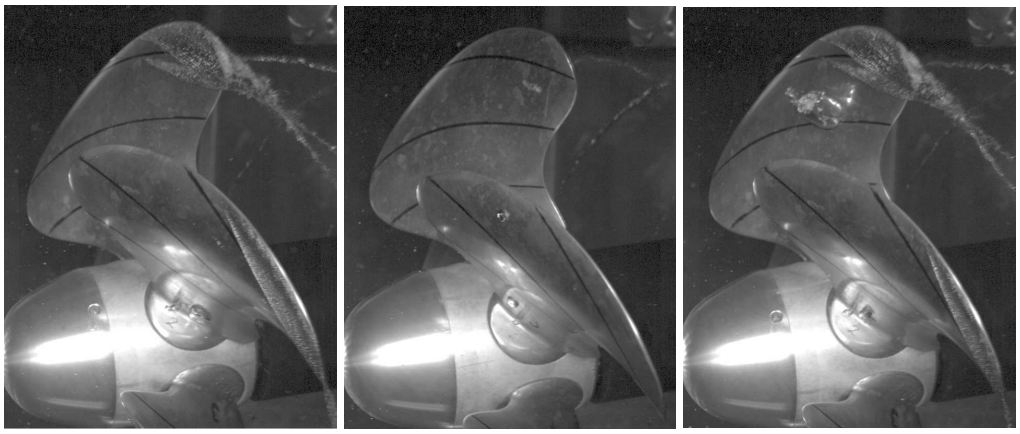

Figure 5.7: Typical cavitation patterns recorded in the experiments, $J = 0.85$, $\sigma = 2.0$. Left frame: typical cavitation pattern; middle frame: strip like cavitation (upper blade) and traveling bubble (lower blade); right frame: typical cavitation pattern with collapsing bubble.

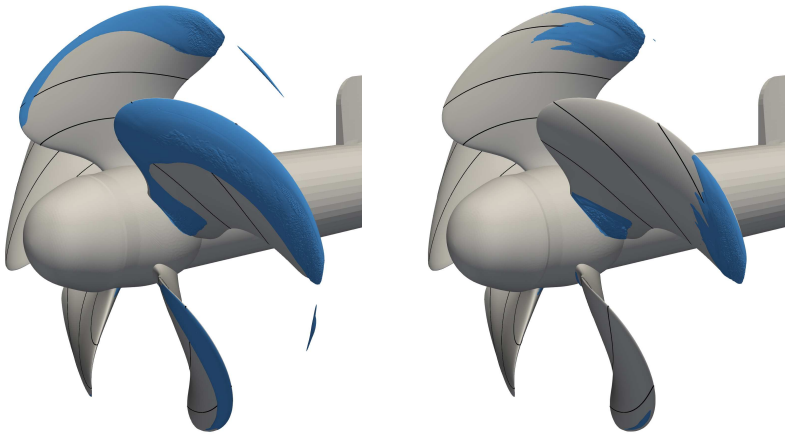

Figure 5.8: Predicted cavitation patterns. $\alpha_v = 0.5$, $J = 0.85$, $\sigma = 2.0$. Left frame: $k-\omega$ $SST+SS$; right frame: bridged model.

6

Cavitating condition pressure pulses

6.1 CAVITATION PREDICTION

The predicted cavitation patterns for the conventional container vessel are shown in figure 6.1, with representative experimental observations and numerical predictions using IDDES under the TS condition which is similar to experimental configurations. The blade positions are accounting from 0 degrees at 12 o'clock position and increasing anti-clockwise viewing from the upstream side, which is the same as the rotation direction.

In figure 6.1, the predicted cavitation patterns with iso-surfaces of Q criterion and experimental cavitation observations are shown at 3 blade positions; in figure 6.2 the cavity structures are plotted transparently with line contours of propeller inflow (U_x/U_{in}). Underneath the transparent sheet cavitation outer interface, a wave-like re-entrant jet can be found formed close to the blade leading edge and travels towards blade tip. At blade position of 40 degrees the re-entrant jet reaches the blade tip end, corresponding to the time of the partial collapse of sheet cavitation and the bursting of tip vortex cavitation. It can be mentioned that the induced TVC dynamics between 40 and 60 degrees, are also located at the high inflow gradient region with denser line contours. The formation of the traveling re-entrant jet can be correlated to the convex shaped sheet cavity closure line, as the cavity interface can be regarded as a surface with constant pressure thus the velocity has potential to be perpendicular to the closure line, though the sheet cavitation itself is a rolling structure which introduce some complexities. The strength of the re-entrant jet is thus related to the position of the maximum curved cavity closure line.

This phenomenon is referred to as 'destruction of tip vortex cavitation by re-entrant flow in the sheet cavitation' in [23] which a common phenomena on ship propellers. The convex shaped cavitation closure line can be found widely in published researches both experimentally and numerically, for propellers operating

in a wake including wakes from ship hull or upstream meshes and panels.The re-entrant jet can also be found from numerical studies with transparent plotted cavity surface and the following TVC dynamics. This phenomenon can lead to significant levels of hull pressure pulses, first discussed in [43]. Experimental study in [44] showed the significant influences of wake and wake peak to the bursting phenomenon.

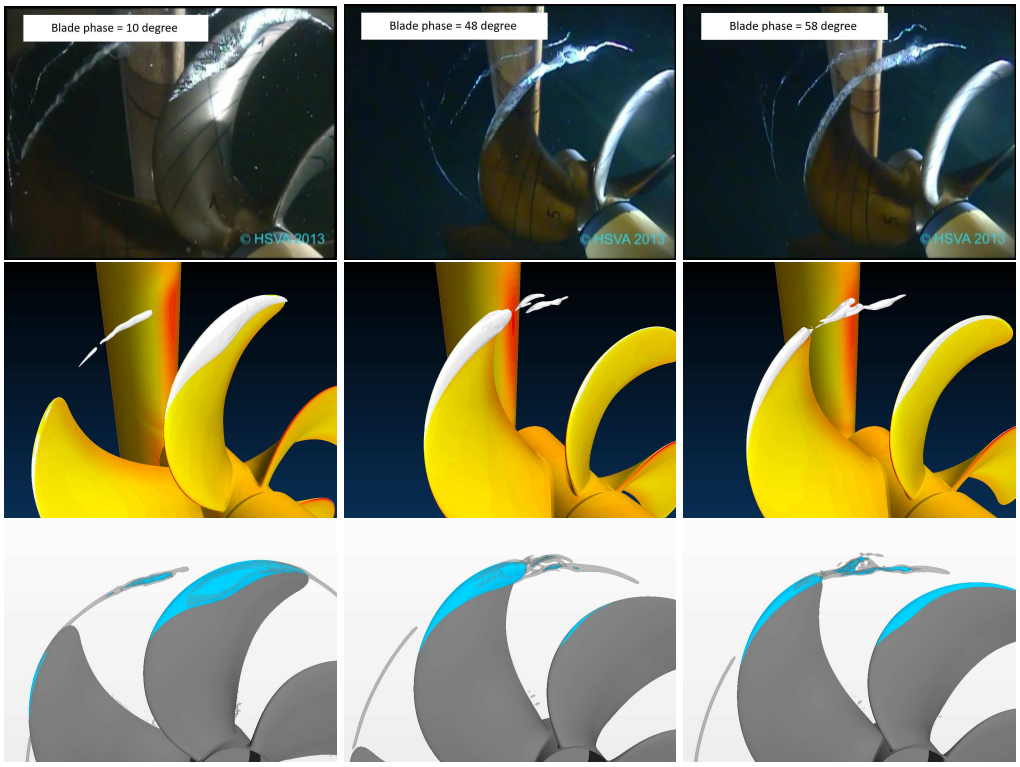

(a) 10° (b) 48° (c) 58°

Figure 6.1: Predicted cavitation patterns, iso-surfaces of Q = 5 $\times$ 10^6 and comparison with experimental recordings.

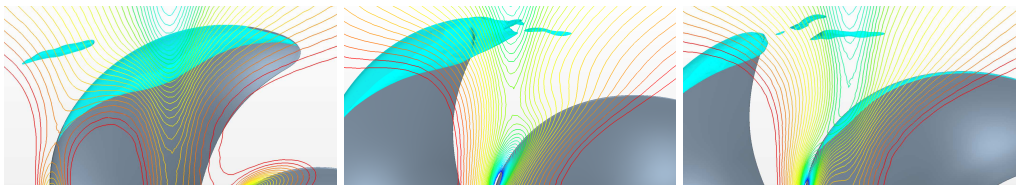

(a) 10° (b) 40° (c) 52°

Figure 6.2: Cavitation and re-entrant jet developments with propeller inflow (U_x/U_{in}) line contours.

The shown experimental cavitation observations are selected representative frames. In figure 6.3, instances are shown for cavitation observations at the same

blade position at different revolutions. The shape and extent of sheet cavitation can differ largely between revolutions. The variations can be related to sheet cavitation inception, shown in figure 6.4. The inception difference on the right hand side blade can lead to different sheet cavitation formations and furthermore, influence the formation of the under-neath re-entrant jet and lead to variations of sheet cavitation collapse as well as TVC formation and bursting, both in magnitudes and phases. This variation will influence hull pressure pulses and radiated noise: reflecting on pressure pulse or noise spectrum, the spectrum broadband levels are expected to be increased with decreased tonal values.

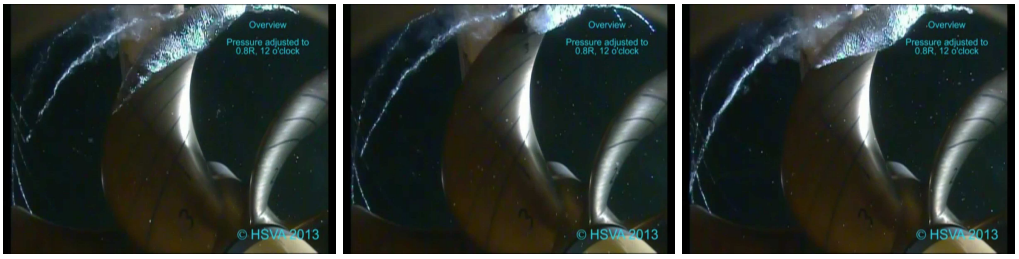

Figure 6.3: Cavitation differences observed in the experiments.

Figure 6.4: Instances of sheet cavitation inception (the right hand side blade).

The predicted cavitating condition hull pressure pulses in paper A are shown in figure 6.5 and figure 6.6, which are predicted using both Star-CCM+ and OpenFOAM under both condition A and condition B using RANS approach, with the tip refined mesh and the base mesh. The predictions in paper E, comparing the predictions using IDDES under TS condition and LD condition are shown in figure 6.7. It is found that for conditions similar to experimental configuration, the predicted hull pressure pulses agree generally well comparing to experimental measurements. A general trend is that at first and second BPF hull pressure pulses agree very well with higher amplitude predictions at higher harmonics, partly due to the highly repeatable cavitation patterns between revolutions in numerical predictions and varying cavitation patterns in the experiments. Without resolving the tip vortex cavitation, stronger sheet cavitation partial collapse will be predicted and the first and second harmonics hull pressure pulse will be slightly over-predicted with lower levels predicted for higher harmonics of BPF.

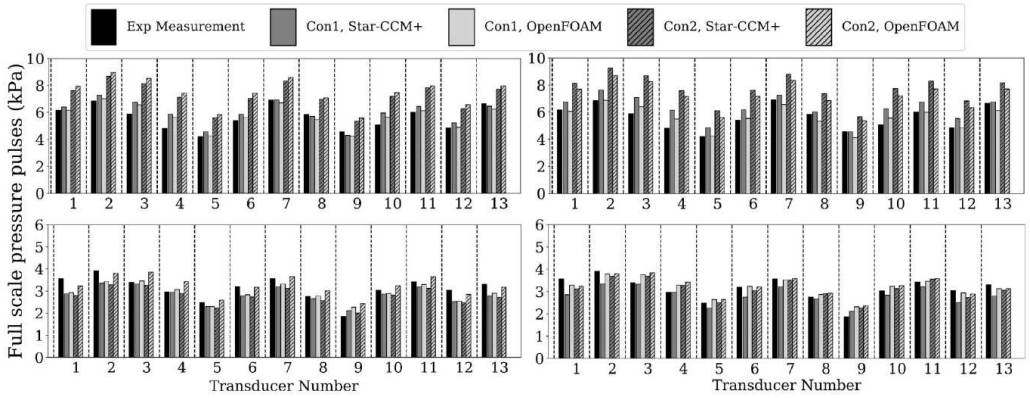

Figure 6.5: Predicted BPF (upper row) and second harmonics (lower row) pressure pulse levels using tip refined mesh (left) and base mesh (right).

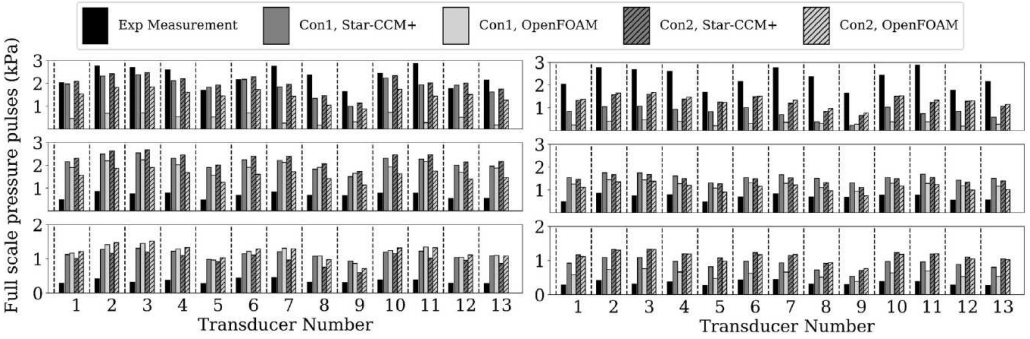

Figure 6.6: Predicted third to fifth harmonics pressure pulse levels using tip refined mesh (left frame) and base mesh (right frame).

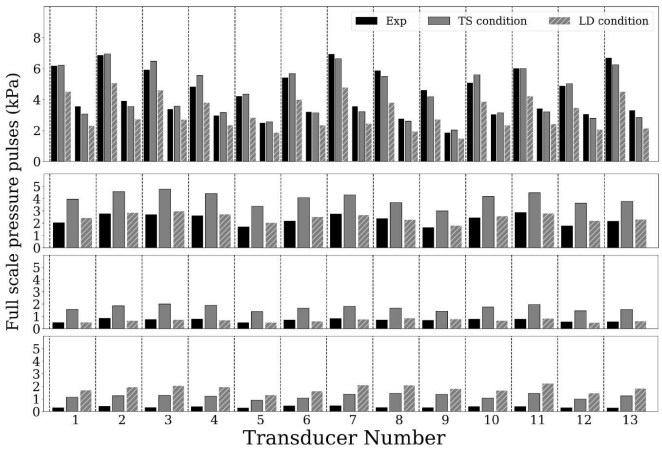

Figure 6.7: Predicted hull pressure pressure levels and comparison to measurements. From top to bottom: first and second harmonics; third harmonics; fourth harmonics; fifth harmonics of BPF pressure pulse levels.

The cavitation patterns and hull pressure pulses are in relation to the predicted propeller inflow. As discussed, its tangential gradient influences the convexity of the sheet cavity closure line and formation of re-entrant jet, and its overall strength influences the general extent of the cavity structure. Shown in figure 6.8, the propeller inflow is generally stronger in studied Condition 2 than Condition 1, which leads to 30% $\sim$ 40% increase of BPF hull pressure pulse.

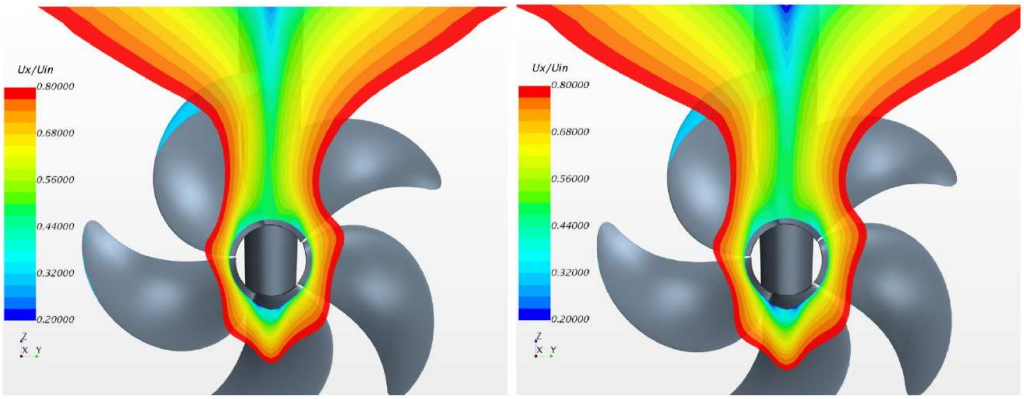

Figure 6.8: Propeller inflow (U_x/U_{in}) 1.7 cm upstream the blade leading edge at the two conditions. Left frame: Condition 1; right frame: Condition 2.

For the cargo ship with LDP, as shown in figure 4.8, the propeller inflow is relatively stronger in model scale simulation and relatively compressed in full scale cases. The different wake predictions result in higher predicted hull pressure pulses in model scale configuration (condition A) comparing to full scale configuration (condition B1). The configuration with hull roughness (condition B2) will also lead to slightly higher predictions. The predictions are shown in figure 6.9 and 6.10. The pressure pulses are highly localized, as an example pressure contour shown in the left frame in figure 3.2; even though the absolute pressure pulse values are high, the integrated force on the vertical direction is moderate, as predicted force fluctuates between 20 kN to 65 kN acting on the area above the propeller center with 1.0 m extension in x direction and 3.2 m extension in y direction. The tip vortex cavitation can be found significant in the experimental observations but not captured in the numerical simulations as no tip region refinement is applied, since the numerical study was performed beforehand experimental study and the cargo ship with LDP is the first case the author studied.

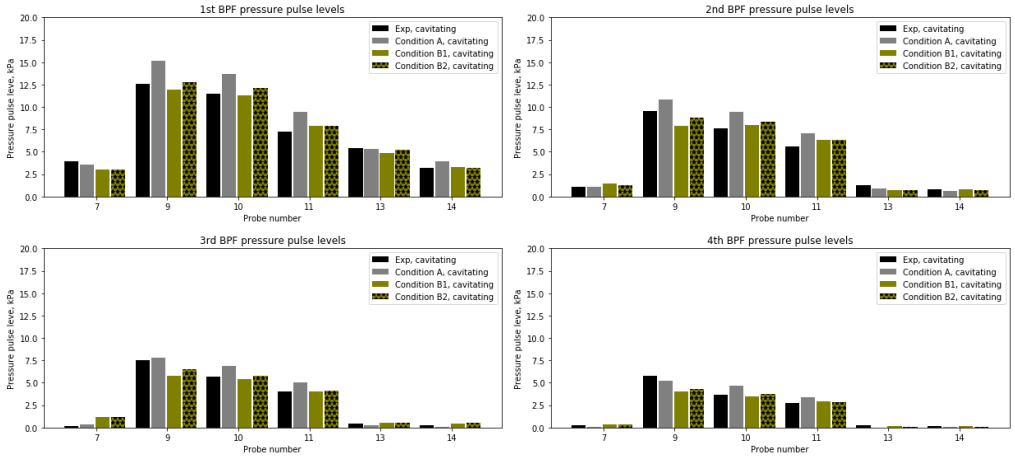

Figure 6.9: Pressure pulse levels on different probe points, cavitating condition.

(a) Exp recording

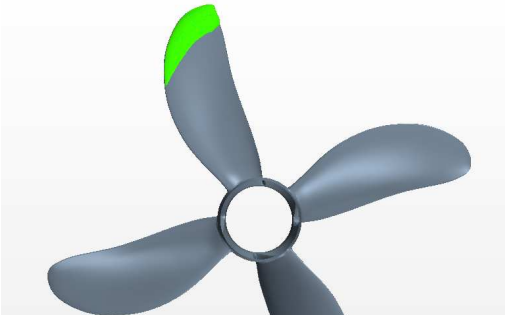

(b) Condition A

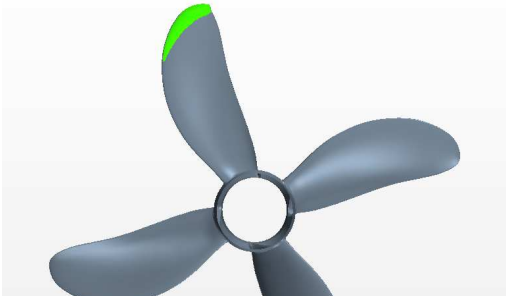

(c) Condition B1

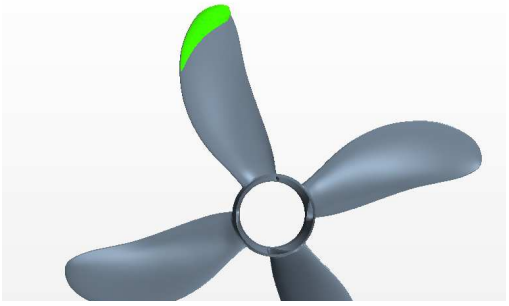

(d) Condition B2

Figure 6.10: Cavitation patterns at blade phase of 22.5 degrees.

6.2 Hull pressure pulses and vapor volumes

There is a close correlation between cavitation induced hull pressure pulses and cavitation vapor volume, and cavitation vapor volume can be recorded during simulation running as the summation of α_v for each cell $V_{total} = \sum \alpha_{v,i} V_{cell,i}$. A stationary spherical monopole source can induce pressure fluctuations omnidirectional and for a far-away given receiver with distance d, the induced pressure

fluctuation p' can be estimated as $p' \approx \frac{\rho}{4\pi d} \frac{\partial^2 V_{(b,t-d/c)}}{\partial t^2}$ under free-field, in which the term $\frac{\partial^2 V_{(b,t-d/c)}}{\partial t^2}$ represents the second order derivative of the breathing monopole volume regarding time. This term can be calculated using the integrated total vapor volume V_{total} without time delay, which is denoted V''_{total} and plotted in the third row in figure 6.11. It is difficult to separate induced pressure fluctuations from different sources, i.e. pressure fluctuations generated by sheet cavitation and TVC. However, the volumes of sheet cavitation and TVC can be separated using a geometrical threshold of wall distance of 2 cm. The deduced V_{TVC} is plotted in blue line in the second frame in figure 6.11, which is very small comparing to V_{total}, while the V''_{TVC} plotted in the bottom frame in figure 6.11 indicating TVC is generating significant levels of hull pressure pulses and rich in higher harmonics.

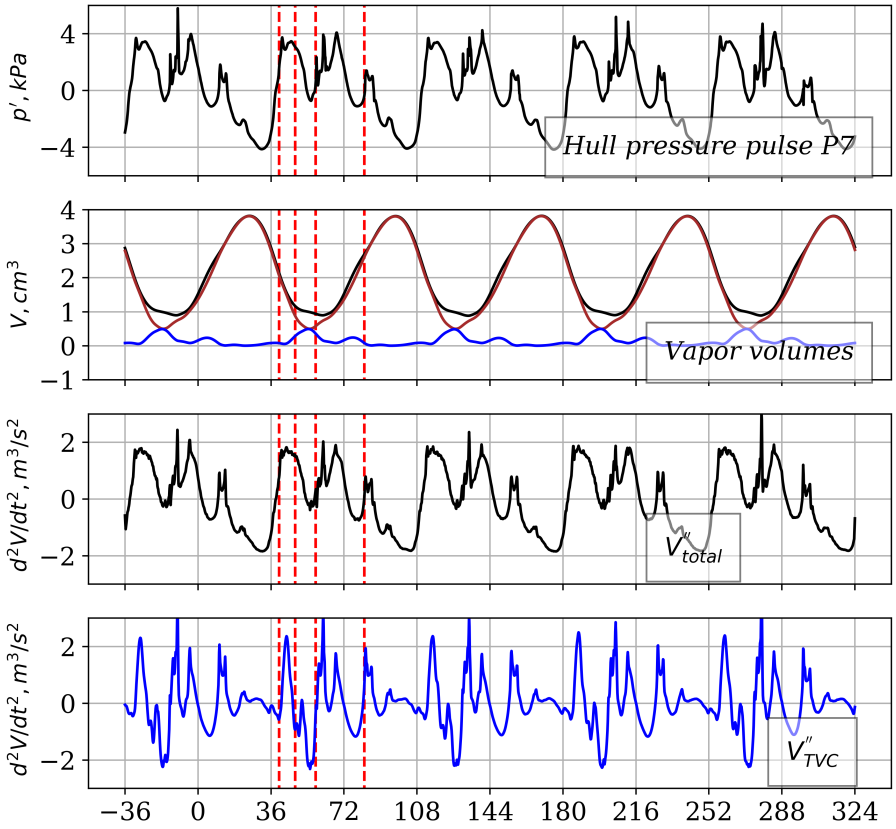

Figure 6.11: Vapor relations with induced pressure fluctuation.

The four blade phases, 40, 48, 58 and 82(10) degrees, are marked as dashed red lines in figure 6.11. Correlations can be found between these marked blade phases and predicted cavitation patterns. Between about 40-48 degrees, when the re-entrant jet reaches the blade end, developing TVC and aft-part collapsing of sheet cavity lead to the first noticeable pressure fluctuation peak. At about 58 degrees, developed TVC starts to collapse and forms the second noticeable peak. Then TVC is rebounding and collapse at 82(10) degrees and forms another

noticeable peak in the pressure signal. The PSDs of V_{total}, and SPL derived from V''_{total} denoted to $p'_{V'',Tran7}$, are shown in figure 6.12. More details can be found in paper A and paper E.

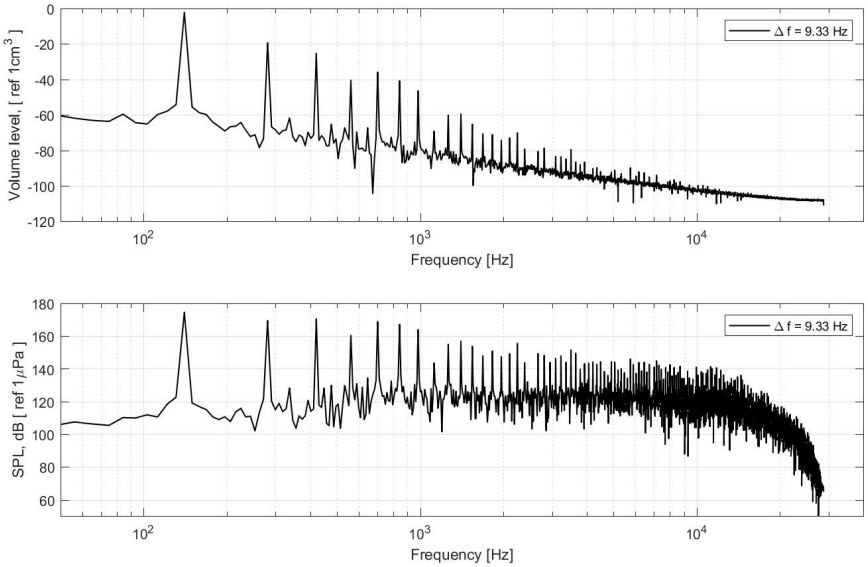

Figure 6.12: V_{total} (top) and $p'_{V'',Tran7}$ (bottom) shown in frequency domain.

7

Ship noise prediction

With satisfying predictions of cavitation patterns and hull pressure pulses, acoustic predictions are further studied for the conventional container vessel. The FWH acoustic analogy with porous data surfaces (PDS) is a natural choice to include the cavitation contribution which is a significant source offset from surfaces. The study was first performed with the TS condition configuration, but the results show that inside the confined space without special damping treatments, the FWH prediction can be problematic due to the violation of free-field Green's function which is the foundation of Farassat 1A derivation. Thus, the simulation domain was changed to a large domain, referred to as the LD condition.

Two different PDS are defined as shown in figure 3.12, $PDS-L1$ encloses the propeller, rudder and the ship wake, while $PDS-L2$ encloses the whole ship including the ship wake. With the incompressible flow input on different defined surfaces the ship noise levels can be predicted for a given receiver. As discussed for the ship noise sea trial, the measured noise levels at far-field (typically >1 Lpp) are scaled to *Ls* corresponding to 1 m distance based on distance normalization assuming spherical acoustic wave spreading ($20log_{10}(d/1m)$ dB) or similar. Thus in numerical predictions the acoustic analogy can predict *Ls* considering varying distant receivers and for receivers located at acoustic far-field, the *Ls* can be expected to be similar using distance normalization where the PDS enclose the most relevant acoustic sources.

However, with incompressible flow solution input, the *Ls* predictions are different from expectations. In short, the direct probed hydrodynamic pressure at a location close to $PDS-L2$, as well as $FWH-PDS-L2$ which took input on $PDS-L2$ using FWH acoustic analogy with receivers close to $PDS-L2$, the predicted noise levels generally agree well with experimental measurements. With receivers placed further and further away from the propeller center, the predicted *Ls* kept increasing and converged with receivers placed 1 km away but to unrealistic high *Ls* levels . Further investigations show that the combination between incompressible solution and FWH acoustic analogy is erroneous.

7.1 HYDRODYNAMIC PRESSURE PREDICTED WITH CFD

For the acoustic predictions, several locations are defined as acoustic receivers, denoted NP1 to NP5k; the distances d from NP1 to NP8 to the propeller center are 1/2.4, $\sqrt{1/2.4}$, 1, $\sqrt{2.4}$, 2.4, 2.4^2, 2.4^3, 2.4^4 in meters, while another two noise receivers at very large distance with d equals to 1 km and 5 km are also considered and denoted NP1k and NP5k. All the receivers are vertically below the propeller center. In the experiments the acoustic hydrophone inside an acoustic chamber connected to the cavitation section, is mounted corresponding to receiver NP5 which is 2.4 m away.

The study first focuses on NP1 which is a few cells away from $PDS-L2$ where the local grid remains fine. The predicted hydrodynamic pressure at NP1 (d_{NP1} = 0.417 m), and at $55\%d_{NP1}$ ($\sim$ 0.23 m), $85\%d_{NP1}$ ($\sim$ 0.35 m), can be directly recorded via direct CFD probing. The predicted Ls in 1/3 octave bands considering the same distance normalization as acoustic wave spherical spreading, as well as comparison with experimental measurements achieved via hydrophone placed 2.4 m vertically below the propeller center inside a connected acoustic chamber, plotted in black solid line considering measured TL and in black dashed line considering distance normalization, are shown in figure 7.1.

At these three probed locations the predicted hydrodynamic pressure is not expected to be influenced by grid coarsening. However, the probed pressure in the incompressible simulation should not be compared with the experimentally measured noise, as in nature the former pressure is hydrodynamic pressure and the latter one should ideally be the acoustic pressure. Besides, in reality the measured acoustic pressure contains many contributions, including pressure induced by propeller thickness and loading effects, non-spherical partly attached cavitation which is also rotating, large size resulting dipole filed from cavitation scattering on solid wall bodies, large size wake field with vortical structures extending long distance downstream and other possible effects. Many of these effects can possibly lead to near-field acoustic pressure contributions and it is not clearly known to what extent these effects can be predicted using the incompressible simulation. But the comparison is still presented here, since in incompressible simulation, a free-field volume mass source induced hydrodynamic pressure fluctuation can be expressed as $\frac{\rho}{4\pi d}\frac{\partial^2 V}{\partial t^2}$ derived from unsteady Bernoulli equation, which is similar to an acoustic monopole source which induce acoustic pressure fluctuation as $\frac{\rho}{4\pi d}\frac{\partial^2 V_{t-d/c}}{\partial t^2}$. Additionally, at NP1, in the incompressible simulation the induced hydrodynamic pressure fluctuation under cavitating condition (fluctuates around $\pm$ 1000 Pa) is much larger than predicted under non-cavitating condition which is simple harmonic wave like around $\pm$ 5 Pa. Back to figure 7.1, the scaled $Ls_{hydrodynamic}$ are consistent based on probed hydrodynamic pressure at $85\%d_{NP1}$ and NP1, but at $55\%d_{NP1}$ the scaled $Ls_{hydrodynamic}$ is different around BPF while consistent at higher frequencies. This indicates at $55\%d_{NP1}$ there are local hydrodynamic effects and at $85\%d_{NP1}$ and $NP1$ (or further locations) the hydrodynamic pressures are not likely influenced by any local hydrodynamic effects and decay

in distance in a similar way of spherical acoustic wave spreading.

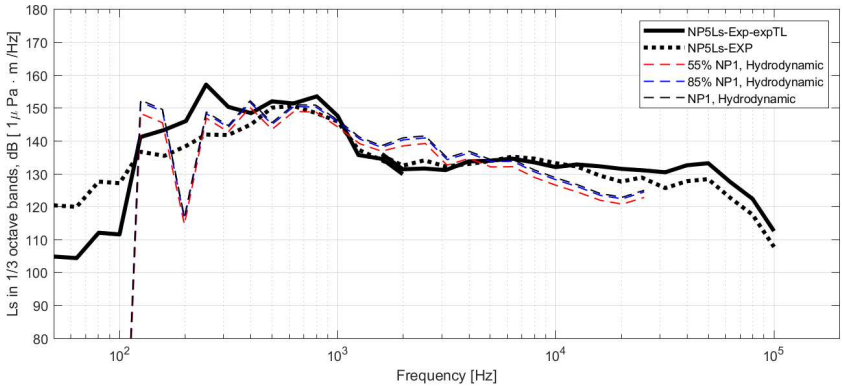

Figure 7.1: Predicted *Ls* based on probed hydrodynamic pressure at 55% d_{NP1}, 85% d_{NP1} and d_{NP1}.

7.2 FWH PREDICTED ACOUSTIC PRESSURES

At NP1, the predicted SPLs of hydrodynamic pressure and acoustic pressure using $PDS-L2$ are shown in figure 7.2 and figure 7.3 respectively. The predicted ship noise source level (*Ls*) in 1/3 octave bands are plotted in figure 7.4. The agreement in the LD condition is generally good between $Ls_{NP1,hydrodynamic}$ and $Ls_{NP1,PDS-L2}$ with acceptable overall shape and trend with maximum difference less than 4 dB around 300 Hz to 500 Hz. For TS condition the difference between the two approaches are noticeable. In figure 7.4, there is another attempt plotted in green dashed line, with *Ls* achieved using the monopole assumption of the cavitation and $S-FWH$ predictions at NP1 on impermeable solid wall boundaries, including the ship hull, rudder, simulation domain top wall and the loading term on the propeller blades.

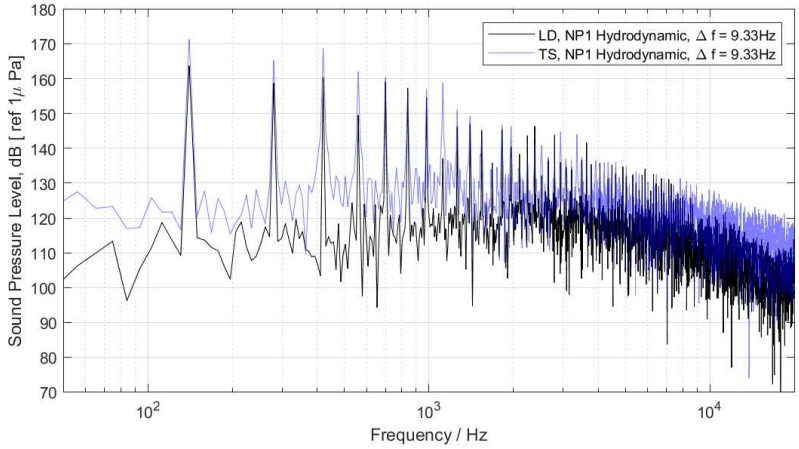

Figure 7.2: *SPL* spectrum with direct CFD probing at NP1.

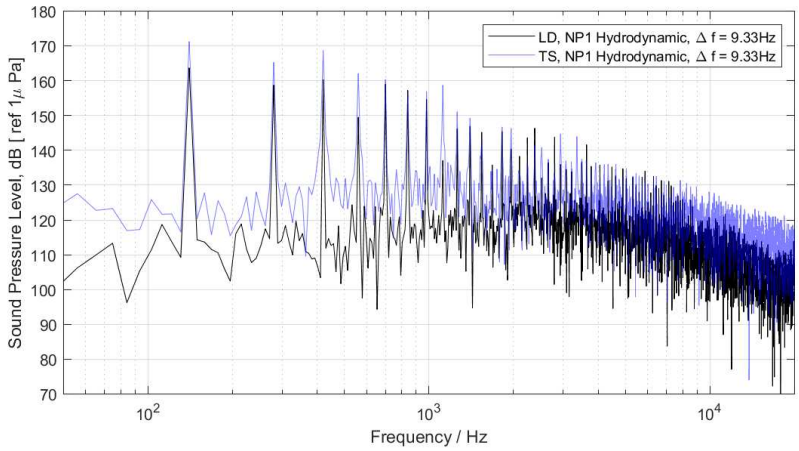

Figure 7.3: *SPL* spectrum with $PDS-FWH-L2$ at NP1.

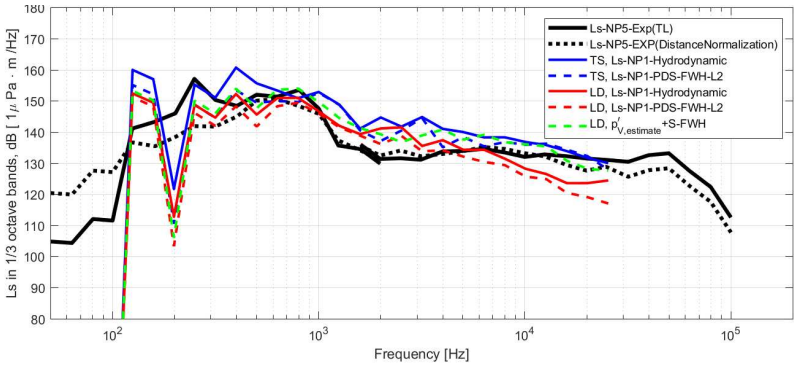

Figure 7.4: Predicted *Ls* in 1/3 octave bands.

7.3 Receiver distance discrepancy

However, using $PDS-FWH$ with receiver NP5, the same position corresponding to the hydrophone placement in the experimental configuration, the predicted *Ls* are plotted as lines with star markers in figure 7.5 and show larger discrepancies comparing to experimental measurements. The discrepancies are increasing with increasing distant receivers considering distance normalization, and converged at NP1k and NP5k, which are located 1 km and 5 km downwards the propeller center. Especially at relatively high frequencies (f $> 1 \times 10^3$ Hz), the difference between Ls_{NP1} and Ls_{NP5k} can be up to 30 dB which is surprisingly large.

These predictions can be further investigated by splitting the pseudo-Thickness and pseudo-Loading terms for $PDS-FWH-L2$ predictions at these noise receivers. The pseudo-Thickness generally follows the scaling of spherical spreading as shown in figure 7.6. Similar to other published results, even though on *PDS* the two terms lost their physical meanings, a similarity can be found between the pseudo-Thickness term with the vapor volume dynamics. However, the focus here

is the pseudo-Loading terms which are shown in the upper frame in figure 7.7 for the studied receiver positions, which are pronounced at higher frequencies and thus likely responsible for what we call *receiver distance discrepancy*. Similarly, the resulting dipole noise, as the scattering on solid walls by the cavity dynamics, can be predicted using the FWH acoustic analogy on the solid walls denoted to $S-FWH$. The Ls_{S-FWH} predictions considering studied receivers are shown in the lower frame in figure 7.7, and similar high frequency noise increases at farther receivers are predicted.

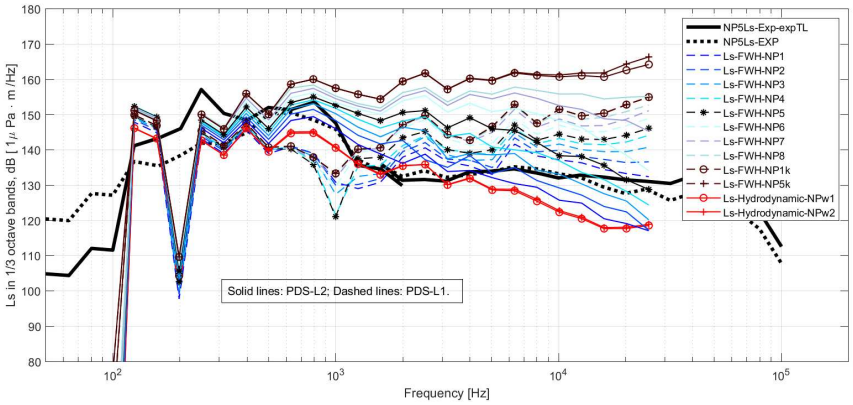

Figure 7.5: *Ls* in 1/3 octave bands based on different receiver locations in LD condition. $FWH-PDS-L2$ results are shown in solid lines and $FWH-PDS-L1$ results are shown in dashed lines.

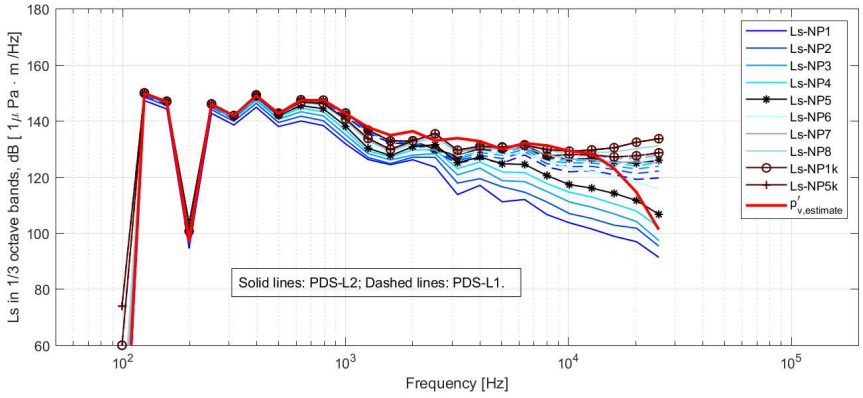

Figure 7.6: *Ls* in 1/3 octave bands based on different receiver locations in LD condition with pseudo-Thickness term. $FWH-PDS-L2$ results are shown in solid lines and $FWH-PDS-L1$ results are shown in dashed lines.

These results suggest the scattering dipole field is responsible for the *receiver distance discrepancy*. This explanation, however, seems strange. According to

the present predictions, a hydrophone need to be placed at least 100 m away for a model scale ship propeller configuration. Besides, if we place a hydrophone at NP1 ($\sim$ 0.4 m away) and NP5 ($\sim$ 2.4 m away) the Ls can differ up to 10 dB, there is no reason that this effect is not observed by experimental researchers and also not reflected on measured TL, which are usually achieved with the ship hull but replacing the propeller with a known transmitter. The limited direct probed $p'_{hydrodynamic}$ suggest that at NP1 the hydrodynamic pressure largely follows the spherical spreading, while here the predicted acoustic pressure using FWH is not, which is also out of expectation. Actually, there are many other possibilities than discussed here, which can be related to numerical errors, quadrupole contributions at relatively far-field claimed in some studies, or the use of incompressible input, etc.

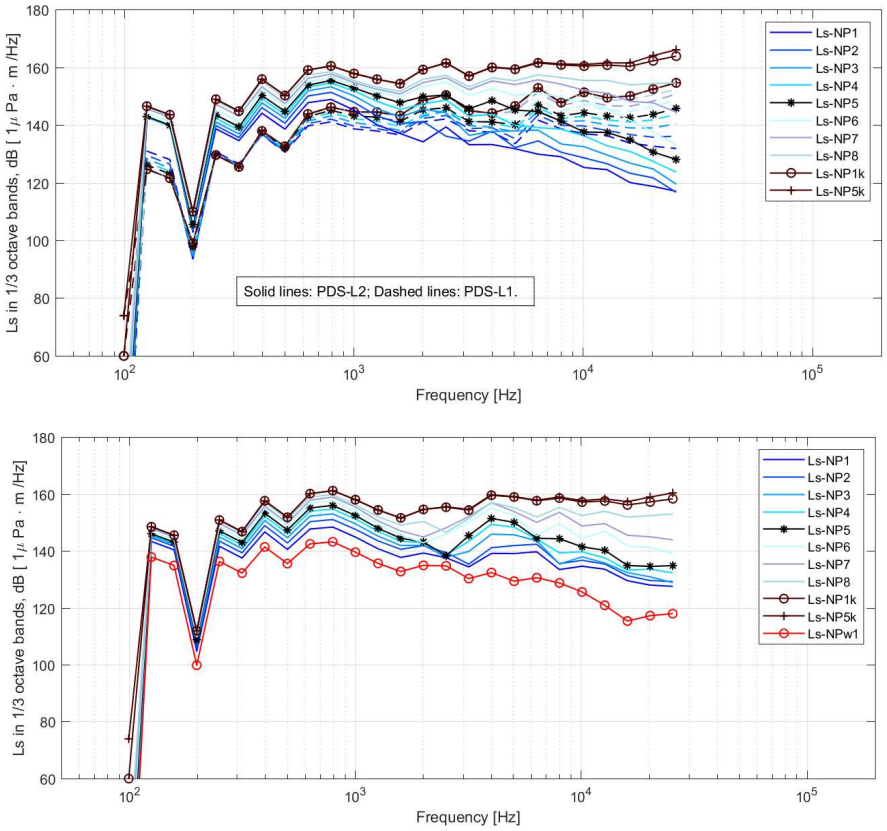

Figure 7.7: Ls in 1/3 octave bands based on different receiver locations in LD condition, pseudo-Loading term using $PDS-FWH-L2$ (upper frame) and $S-FWH$ on solid boundaries (lower frame).

7.4 MONOPOLE TEST CASES

As a further study to the *receiver distance discrepancy* problem, a very simplified case with a stationary standalone monopole source generating noise in free-space, as shown in figure 7.8, is set up. The volume meshed spherical monopole source is derived from the LD condition numerical simulation, i.e. the first order derivative of the integrated total vapor volume V_{total} with radius a = 0.01 m as $\rho_{water}\frac{\partial V_{total}}{\partial t}/(4/3\pi a^3)$, which is plotted in figure 7.9. The volume of the designed monopole is about 4.2 cm^3 which is similar in size to the total vapor volume in LD condition which is about 3.0 cm^3 .

Several PDS were defined for noise prediction using FWH, denoted $PDS-ML1$ to $PDS-ML4$ shown in figure 7.8. $PDS-ML1$ is a source centered sphere with radius a = 0.1 m; $PDS-ML2$ is a source biased positioned box; $PDS-ML3$ is a source centered sphere with radius a = 2.3 m and $PDS-ML4$ is a source centered cubic box with an edge length of 5.2 m.

The size of the computational domain is very large with a cubic box with an edge length of 260 m. The simulations were run for 0.07 s, equivalent to the time of 2 propeller revolutions with data collection for the second revolution time. For the compressible solver there is no special treatment on the outer boundaries as the domain is large enough to avoid possible reflections during this limited time. For the incompressible simulation, the six outer patches are set to mass flow input boundaries with mass flow calculated based on the input monopole source, to guarantee mass conservation in the simulation domain. The maximum target cell length is 0.02 m inside $PDS-ML4$; as shown in the figure the cells have similar characteristic length for the spaces between $PDS-ML2$, $PDS-ML3$ and $PDS-ML4$. There are in total 18.8 million cells for this simple test case, generated using Star-CCM+ built-in polyhedral mesher.

For both compressible and incompressible simulations, a standard CFD approach is used with laminar segregated flow using second-order implicit time scheme for time advancing. Constant density is used for the incompressible simulation, while IAPWS-IF97 is used for the compressible solver with isothermal model; however no isothermal condition was necessary to configure and solve for.

Assuming a monopole source in free-space, the major difference between incompressible and compressible assumptions is the wave propagation speed which will influence the retarded time for source computation. For a receiver in space, the incompressible solution and compressible solution will ideally have the same shape and magnitude, but with a time shift. Thus for a receiver point, the directly probed noise spectra are expected be the same. However, if we consider a *PDS* to feed FWH, the *PDS* consists of elements with different distance relative to the monopole source, there will be phase shifts of the signal at each face on the *PDS* using the incompressible solver compared to the compressible solution or in physical reality. The only exception is a sphere-centered PDS, similar to the $PDS-ML3$ in figure 7.8 where there is no relative phase shift between faces. This leads to the expectation that with incompressible solution,

only $PDS-FWH-ML3$ will provide correct noise prediction using FWH; while with compressible solution all the PDS will provide correct noise prediction using FWH as well as direct probing. To highlight this, the comparison between $PDS-ML2$ and $PDS-ML3$ will be shown in details. The two PDS are located in regions with the same cell size, and furthermore, even though numerical error should be very small for this kind of simple case, the hydrodynamic predictions on $PDS-ML2$ should be more accurate than $PDS-ML3$ as it is closer to the only source.

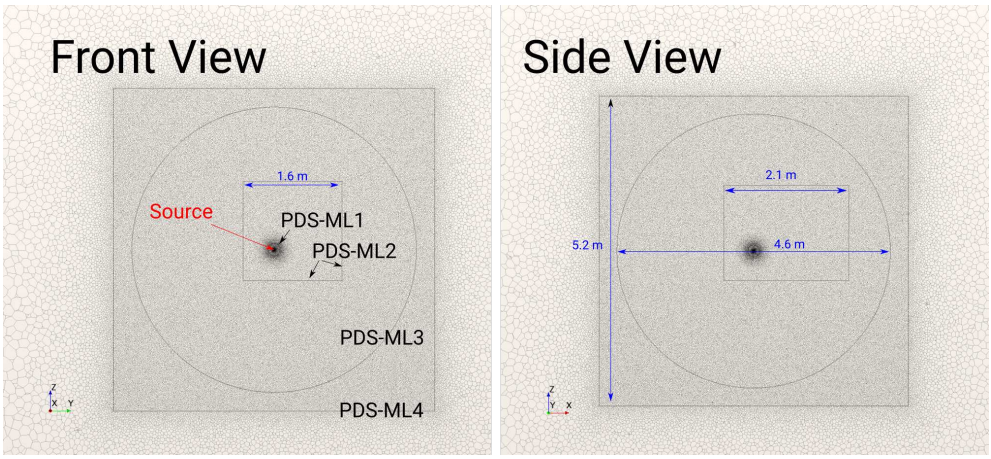

Figure 7.8: The free-field monopole with $PDS-FWH$ placements.

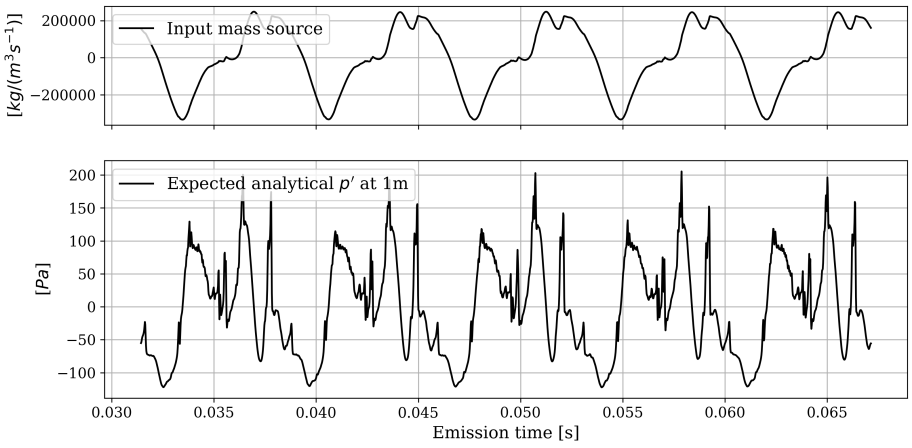

Figure 7.9: Input mass source (upper) and expected analytical p' at 1 m distance (lower).

Using $PDS-ML2$ and $PDS-ML3$, the predicted Ls with receiver NPM3, NPM4, NPM5 and NPM6 are summarized in figure 7.10; these receivers are located at 1 m, 10 m, 100 m and 1000 m from the source center. For the compressible simulation, the predictions are very similar except that $PDS-FWH-ML3$

predict an earlier decay at higher frequencies, presumably due to numerical diffusion. Over-lapping predictions can be found for each PDS irrespective of considered receiver locations. However, as shown in figure 7.10, the over-predictions are very clear with the incompressible solution using $PDS-ML2$ with increasing receiver distance while using $PDS-ML3$ there is no such kind of over-prediction at higher frequencies. Further, it should be noted that for a closer receiver location NPM3, located close to $PDS-ML2$, less influence is noted using the incompressible solver. This is since at a closer receiver, the FWH predictions are more weighted on the smaller region on *PDS* close to the receiver, where relatively smaller phase shifts occur.

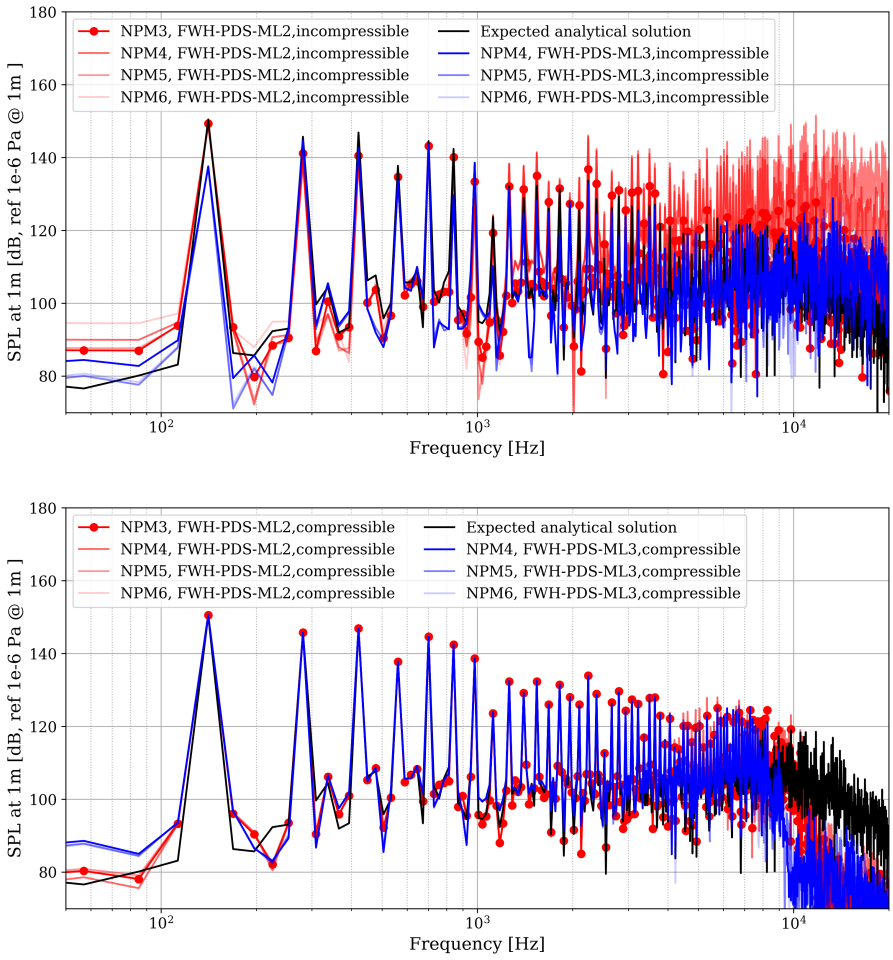

Figure 7.10: Predicted scaled *SPL* using $PDS-FWH-ML2$ and $PDS-FWH-ML3$ with different receivers; incompressible input (upper frame) and compressible input (lower frame).

If looking at *Ls* in 1/3 octave bands, as summarized in figure 7.11, clearly using $PDS-ML2$ with FWH and incompressible solutions, over-predictions can be noticed with increasing frequencies. The *receiver distance discrepancy* is rather

well reproduced: the *Ls* start to increase at around 1 kHz about 10 - 15 dB and increased to 30 dB at around 10 kHz. The results of $PDS-ML2$ here explains the increasing over-predictions using $PDS-L1$, $PDS-L2$ and $S-FWH$ in the ship configuration simulations. For using compressible solver or the incompressible solver with $PDS-FWH-ML3$, the center positioned sphere, predicted *Ls* generally agree well compared to the input source. However, for the configuration with ship and cavitating propeller, there is no similar porous data surfaces similar to a center positioned sphere. Besides, even using a center positioned spherical *PDS*, the combination between incompressible solver and FWH can lead to inaccurate noise predictions, as observed in figure 7.10 the BPF noise is noticeably under-predicted due to different governing equations and velocity predictions between incompressible solver and compressible solver.

In short, for using incompressible solution with $PDS-FWH$, it was found that the predicted noise source levels are dependent on the shape of *PDS*, the distance from source to *PDS* and the distance from receiver to *PDS*; while in certain combinations the error is relatively small, with small *PDS* and receiver closer to the *PDS*. These dependencies are not observed using compressible solution, other than numerical diffusion.

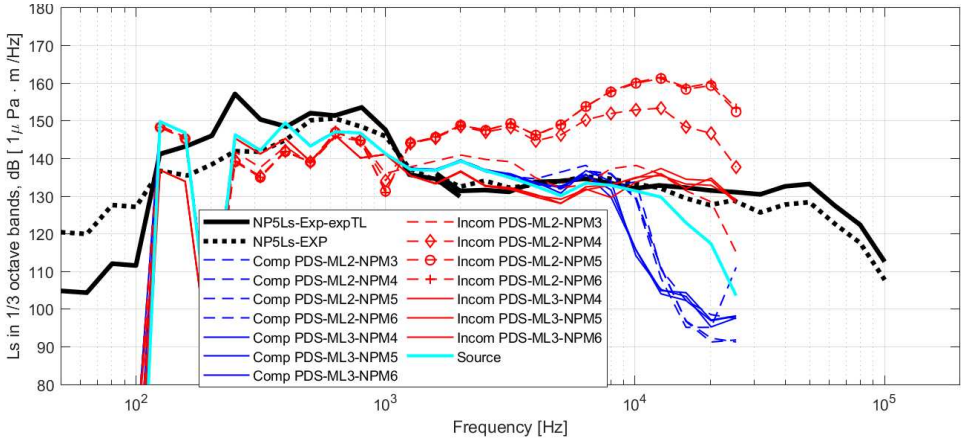

Figure 7.11: Predicted *Ls* using $PDS-ML2$ and $PDS-ML3$ at different receivers using compressible and incompressible solver and comparing to the expected analytical solution.

Furthermore, as shown in figure 7.10 using the spherical $PDS-ML3$, the high frequency over-predicitons are avoided but there is still noticeable differences at BPF between incompressible and compressible input. It can be estimated according to the diameter of $PDS-ML3$ which is 2.3 m, the delay of compressible solution is about 88 timesteps. Thus the time steps are adjusted and the scaled p' using $PDS-ML3$ with both incompressible and compressible solvers are shown in the upper frame in figure 7.12. The compressible solution of predicted noise in time history agrees with analytical solution while components are missing for the incompressible solution.

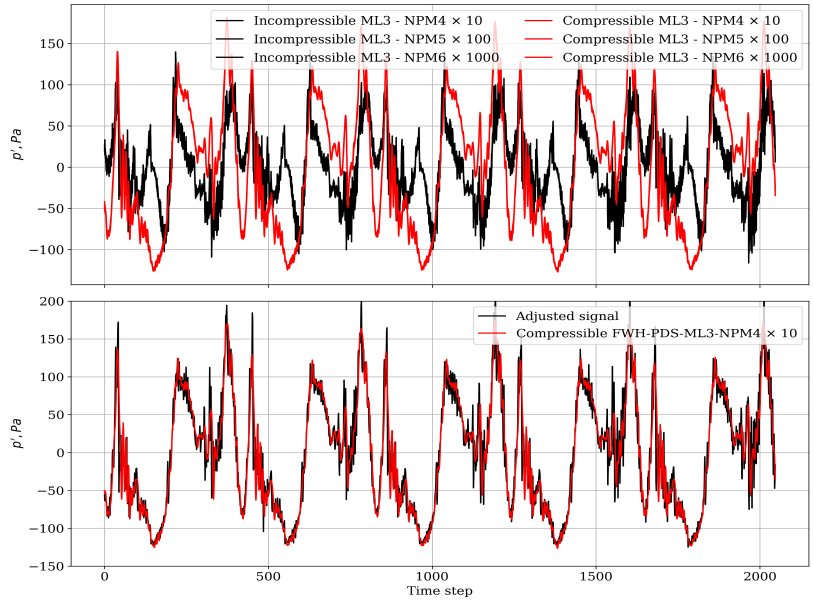

Figure 7.12: Scaled p' predicted using $FWH-PDS-ML3$ at different receivers (upper) and adjusted signal using first-order derivative of incompressible pseudo-Thickness term (lower). Phase shift adjusted.

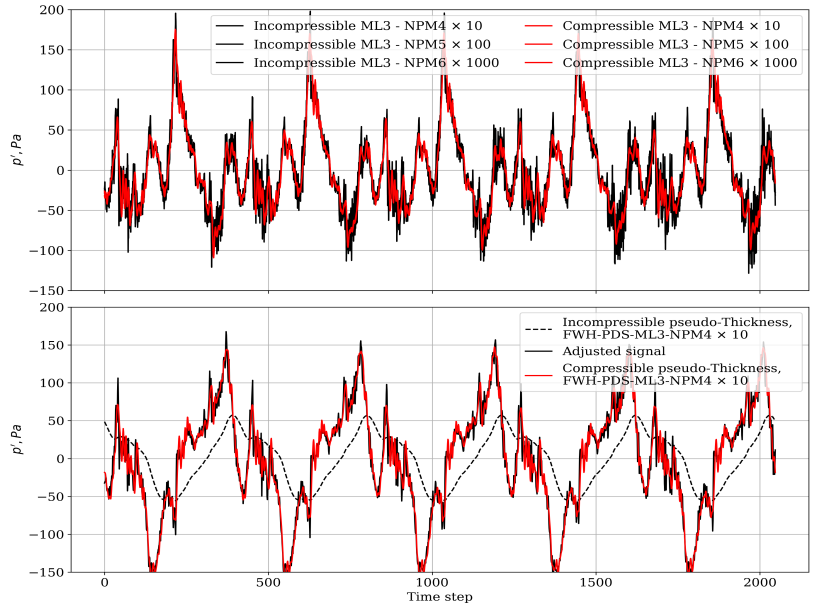

Figure 7.13: Predicted pseudo-Loading terms (upper frame) and pseudo-Thickness terms with corrections (lower frame).

The pseudo-Loading term agree well between incompressible and compressible solution shown in figure 7.13, and the difference comes from the pseudo-Thickness term, plotted in black dashed lines in the lower frame in figure 7.13 for incompressible solution; the terms for the compressible solution are plotted in

red lines. An interesting observation is that the difference between the two can be likely filled with the scaled first-order derivative of the incompressible pseudo-Thickness term with a factor of 0.015 for using $PDS-ML3$, and the corrected signals are plotted in black lines in the lower frame of figure 7.13 and 7.12 for the corrected pseudo-Thickness term and the total noise signal. The results indicate that apart from the relative phase shifts between elements on a PDS, incompressible solution predicted different velocities especially on a PDS away from the source, due to simplifications introduced by constant density to the governing equations.

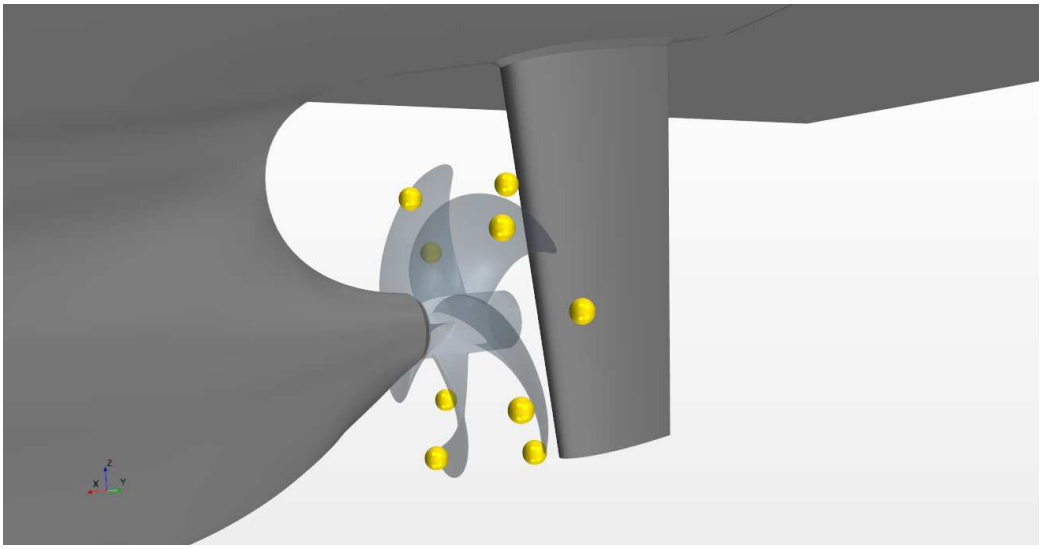

Figure 7.14: Designed case RM with rotating monopoles representing sheet can tip vortex cavitation for the 5 blades. The removed propeller is shown transparently.

As the last part of the monopole test case and a closure of noise related study, a designed case, referred to case RM is shown in figure 7.14. The simulation domain and PDS placements are same with the ship LD condition simulation configurations, while the propeller is removed and replaced by 10 monopoles. These 10 monopoles are rotating in the same way as the removed propeller, 5 of them representing sheet cavitation on the 5 blades, and the other 5 monopoles representing the TVC of the 5 blades. The solver settings are similar to the free-field monopole test case with laminar treatment and without inflow. The resulting *SPL* are shown in figure 7.15 using incompressible solver and compressible solver. The simulation is intended to represent the ship configuration simulated in LD condition, and it can be found that using incompressible input the *receiver distance discrepancy* is reproduced again, while for the compressible input the predicted noise levels are inline with expectations, with likely slight differences of broadband noise predicted using varying distant receivers and distance normalization. There are in total 6.22 million cells in the simulation domain, and the simulation is less in quality comparing to other performed cases. It can be noted that the

difference of predicted hull pressure pulses between compressible case and incompressible case is very small, but show smaller spatial variations between the transducers comparing to LD condition simulations. Test was made for incompressible solution with inflow and propeller blades, predicted hull pressure pulses thus agreed well with LD condition predictions, but not clearly known if it is the cavity scattering effect on the blades or the thickness and loading effects of the propeller blades lead to this differences.

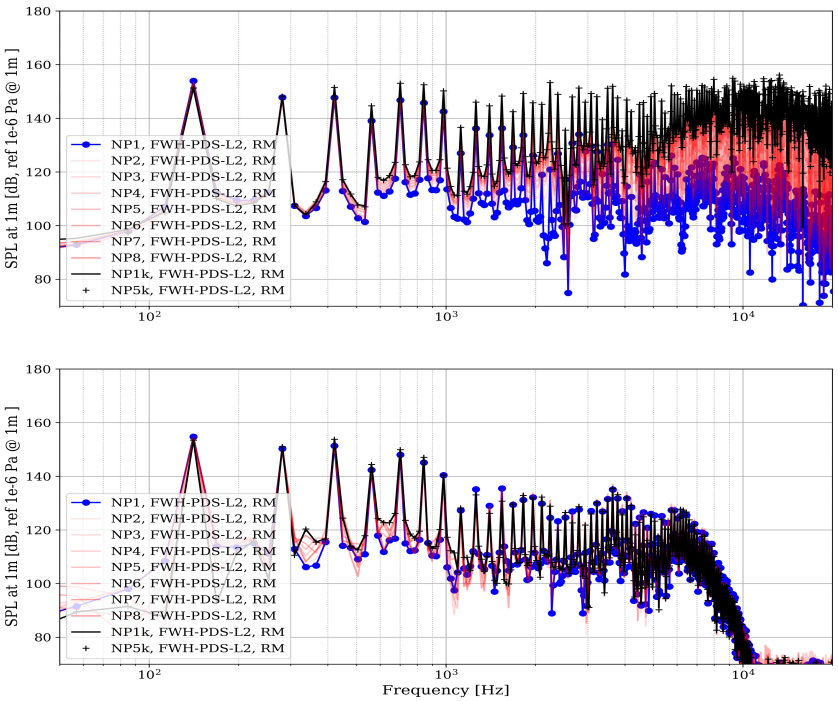

Figure 7.15: Predicted *SPL* at 1m using the incompressible input (upper frame) and compressible input (lower frame) based on varying distant receiver.

Summary of monopole test case observations

To sum up the observations using the monopole test case, the following can be noted.

1. There are two noticed problems using the incompressible input on PDS with the FWH acoustic analogy: the first one is the missing of acoustic wave traveling time from the acoustic source to the PDS; the second one is the predicted flow quantities on the PDS that are different compared to the compressible solutions. The first problem may lead to increased high frequency noise while the latter may lead to decreased noise levels.

2. For a given (compact) monopole acoustic source, the predicted *Ls* should be independent on the location of PDS placements or receiver locations; while using the incompressible input the predicted *Ls* is dependent on these factors. For predictions with compressible input, the summation of pseudo-Thickness and pseudo-Loading terms are kept constant if scaled with distance, but the relative

importance of the two are changing depending on the distance from the source to the PDS; the pseudo-Loading term is relatively small for a PDS close to the source but increasing with PDS placed further away to the source. For predictions with incompressible input, the general trend is similar but the summation of the two terms are varying.
3. With the incompressible input, a PDS close to the source lead to very little differences and providing very similar predictions comparing to compressible predictions. With a PDS placed away from the source, the relative phase shifts between elements on PDS become significant and the resulting erroneous high frequency noise increase mainly comes from the pseudo-Loading term. The relative importance of the pseudo-Loading term is also increasing with PDS placed further away to the source. This can be overcome by using a source centered spherical PDS. For a non-spherical PDS, a receiver placed very close to the PDS is less influenced, since a very close receiver can be dominated by a relatively smaller region on the PDS.
4. The prediction of pseudo-Thickness term can be found different using compressible and incompressible input. For a PDS close to the source the difference is small, and increasing with increasing distant PDS. The difference is observed largely by the prediction difference of velocity between compressible and incompressible flow predictions.
5. For the ship configuration with a cavitating propeller, there is no 'source centered spherical PDS' due to the non-compactness of the rotational cavity structures. The PDS can not be small to encloses only the propeller which is located inside the large size cavitation scattering dipole field of the ship hull. Using $S-FWH$ for the this cavitating case can be problematic as well, as the equivalent dipole field on the ship hull and other solid boundaries will have the same phase shift problem. For cases with flow noise generated close to the surface, the discussed problems are expected to be insignificant using $S-FWH$.

8

Concluding Remarks

Non-cavitating pressure pulses

The tip clearance can be of vital importance inducing high levels and high frequency hull pressure pulses, as revealed in the studied case of the general cargo vessel with LDP. Higher harmonic components of pressure pulses are not coming from tip vortex dynamics as is normally argued, but from the short duration pressure peaks when the blade is passing close to the hull. The short pressure peaks resulted similarly to a signal with repeated unit impulses and FFT analysis of a this signal will lead to high frequency components.

Apart from this relatively unique case, under non-cavitating conditions the induced pressure pulses are dominated by BPF components. According to the studied case of the Kongsberg propeller A mounted on inclined shaft, there is only subtle prediction differences comparing a very coarse mesh (7.2 million cells) to a fine mesh (26.3 million cells). For the case using a transitional sensitive turbulence model, several percents of K_T difference can be predicted comparing with predictions using the $k-\omega$ *SST* turbulence model, while there is still only subtle differences for the predicted BPF pressure pulses. The tip vortex is neither likely to influence the non-cavitating hull pressure pulse, as shown in the studied container vessel case via the comparison between the base mesh and tip refined mesh; the two configurations predicted rather different tip vortex structures but similar BPF pressure pulses. The non-cavitating pressure pulses are dependent on operating conditions and general configurations in numerical settings and experimental settings.

Cavitation and cavitating pressure pulses

Cavitation typically leads to significant levels of pressure pulses. The studied case of the container vessel show that cavitation structures generate pressure fluctuations in a monopole way as the second order-derivative of the total vapor volume regarding time, $p' \approx \frac{\rho}{4\pi r}\frac{\partial^2 V_{vapor}(t-r/c)}{\partial t^2}$. The estimated pressure pulses generated

by sheet cavitation and tip vortex cavitation, via separation of cavitation vapor volumes, show the sheet cavitation mainly contribute to pressure pulses at lower BPFs and tip vortex cavitation contribute to pressure pulses rich in higher harmonics. The study also revealed mechanisms of tip vortex cavitation bursting, which is a common phenomenon observed on ship propellers and resulted from the interaction between sheet cavitation, re-entrant jet underneath sheet cavity and tip vortex cavitation dynamics.

Sheet cavitation

Sheet cavitation is one of the major sources inducing pressure pulses and it is believed to be contributing to mainly first and second BPFs, and higher harmonics pressure pulses can be induced by possible transient cavitation dynamics. The ship wakes that the propellers are operating in, can lead to different pressure predictions on the blade and thus resulting to different sheet cavitation developments and pressure pulses. Without sufficient prism layer cells and mesh resolutions in the wake region, the diffusive wake (propeller inflow) can lead to significantly under-predicted sheet cavitation and induced pressure pulses. The wake differences can also be used to explain the pressure pulse differences under different Reynolds numbers. As shown in the studied case of the general cargo vessel with LDP, in model scale (lower Reynolds number) the wake is generally stronger and in full scale (higher Reynolds number) the wake is more compressed in space; sheet cavitation as well as induced hull pressure pulses can be found relatively more significant in model scale condition. In the studied container vessel case in paper A, the lower Reynolds number condition follows the Froude's law of scaling, stronger wake is predicted and BPF pressure pulses is predicted higher comparing to the operating condition with the higher Reynolds number condition.

Re-entrant jet and tip vortex bursting

TVC bursting and its rebounding are found inducing high levels of hull pressure pulses rich in higher frequencies. The accurate prediction of TVC can be much more computationally demanding with advanced modeling, but in the present study significant TVC dynamics were predicted. The interaction between TVC and sheet cavity is a factor influencing the induced hull pressure pulse. Without mesh refinements in the blade tip region to resolve TVC, the partially collapse of sheet cavity can be predicted stronger and lead to high frequency pressure pulses numerically. The TVC bursting is also found triggered by the traveling re-entrant jet underneath sheet cavity and related to the convexity of the sheet cavity closure line. The convexity of sheet cavity closure line can be further related to the propeller upstream inflow, especially regarding the tangential gradient of the axial velocity. The re-entrant jet can be found reach the blade leading edge instead of the blade tip region, and inducing bursting of leading edge TVC according to one of the other studied case. This phenomena is less common for propellers operating under relatively uniform inflow.

Sheet cavitation inception

The inception of tip vortex cavitation is known to be important as TVC is the first cavitation phenomenon showing up; on the contrary the inception of sheet

cavitation on propeller blades and its relation with laminar-transitional flow is less studied, due to the very high Reynolds number of full scale operating marine propellers and laminar-transitional boundary layer mainly matters under relatively lower Reynolds number. For model scale marine propellers operating under Reynolds number typically ranging between 5×10^5 and 2×10^6, especially with relatively uniform propeller inflow, large blade areas with laminar or transitional boundary layer can exist and suppress the sheet cavitation. The $\gamma - Re_\theta$ transition model based on local flow correlations is used to predict the location of laminar separation and bridged with the Schnerr-Sauer cavitation mass transfer model, and predicted significantly improved sheet cavitation pattern on the studied hydrofoil and model scale marine propellers mounted on inclined shaft. The sheet cavitation suppression by laminar-transitional boundary layer is also suspected to be appearing for operating marine propellers operating behind the model scale ship hull. An effective way to overcome the issue on the experimental side is to apply roughness on propeller blade leading edge.

Ship noise

The predictions of far-field ship noise are studied using FWH acoustic analogy with different porous/permeable data surfaces (PDS) and incompressible flow solution input, for the model scale container vessel operating in a large simulation domain. The predicted ship noise source levels *Ls* are abnormal. The investigation using a free-field representative monopole shows clear indications that the combination between incompressible solution and $PDS-FWH$ is erroneous, which mainly comes from the missed acoustic traveling time from acoustic source to the PDS and resulting in unrealistic noise level increases at high frequencies, while the differences of flow predictions between incompressible solution and compressible solution also contribute to the error. With a small PDS or spherical PDS enclosing a compact monopole source the error can be small using incompressible solution input, but for the ship configuration with a rotating propeller these PDS placements can not be achieved. A receiver placed close to the PDS is less influenced by the retarded time differences between elements on the PDS, and $PDS-FWH$ predictions with PDS encloses the whole ship configuration are generally agreed with direct probed incompressible hydrodynamic pressure as well as experimental measured noise source level.

For the studied container vessel, the most significant acoustic source is the predicted cavitation dynamics, while the resulting dipole fields on the ship hull and other solid boundaries also contribute. The loading and thickness effects of the rotating blades are comparatively less significant. The turbulent wake can be found extending a long distance downstream the rudder. For cases with flow noise generated close to the surface, $S-FWH$ can be used for noise predictions with incompressible solver, but for a cavitating marine propeller with scattering on ship bodies neither $PDS-FWH$ nor $S-FWH$ can be used for far-field noise prediction with an incompressible solution.

REFERENCES

[1] G. V. Frisk, "Noiseonomics: The relationship between ambient noise levels in the sea and global economic trends," *Scientific reports*, vol. 2, no. 1, pp. 1–4, 2012.

[2] J. Tournadre, "Anthropogenic pressure on the open ocean: The growth of ship traffic revealed by altimeter data analysis," *Geophysical Research Letters*, vol. 41, no. 22, pp. 7924–7932, 2014.

[3] R. M. Rolland, S. E. Parks, K. E. Hunt, M. Castellote, P. J. Corkeron, D. P. Nowacek, S. K. Wasser, and S. D. Kraus, "Evidence that ship noise increases stress in right whales," *Proceedings of the Royal Society B: Biological Sciences*, vol. 279, no. 1737, pp. 2363–2368, 2012.

[4] C. M. Duarte, L. Chapuis, S. P. Collin, D. P. Costa, R. P. Devassy, V. M. Eguiluz, C. Erbe, T. A. Gordon, B. S. Halpern, H. R. Harding, M. N. Havlik, M. Meekan, N. D. Merchant, J. L. Miksis-Olds, M. Parsons, M. Predragovic, A. N. Radford, C. A. Radford, S. D. Simpson, H. Slabbekoorn, E. Staaterman, I. C. Van Opzeeland, J. Winderen, X. Zhang, and F. Juanes, "The soundscape of the Anthropocene ocean," *Science*, vol. 371, no. 6529, 2021.

[5] L. Bedriñana-Romano, R. Hucke-Gaete, F. A. Viddi, D. Johnson, A. N. Zerbini, J. Morales, B. Mate, and D. M. Palacios, "Defining priority areas for blue whale conservation and investigating overlap with vessel traffic in chilean patagonia, using a fast-fitting movement model," *Scientific reports*, vol. 11, no. 1, pp. 1–16, 2021.

[6] "Underwater acousticsquantities and procedures for description and measurement of underwater sound from ships part 1: Requirements for precision measurements in deep water used for comparison purposes," *ISO 17208-1: 2016. International Organization for Standardization Geneva, Switzerland*, 2016.

[7] "Underwater acousticsquantities and procedures for description and measurement of underwater sound from ships part 2: Determination of source levels," *ISO 17208-2: 2019,International Organization for Standardization Geneva, Switzerland*, 2019.

[8] "Ships and marine technology - measurement and reporting of underwater sound radiated from mechant ships - survey measurement in deep-waters," *ISO/DIS 16554.3, International Organization for Standardization Geneva, Switzerland*, 2014.

[9] "Procedures for description and measurement of underwater sound from ships–part 1: General requirements," *American National Standard ANSI/ASAS*, 2009.

[10] "Ittc recommended procedures and guidelines. underwater noise from ships, full scale measurements," *ITTC Quality System Manual*, 2017.

[11] "Part 6, chapter 24, silent class notation, rules for classification of ships," *DNV/GL*, 2017.

[12] "Gd28-2018," *China Classification Society*, 2018.

[13] "D3.1, european urn standard measurement methods," *Achieve QUoieter Oceans by shipping noise footprint reduction*, 2014.

[14] "Final report and recommendations to the 28th ittc," *Proceedings of 28th ITTC: The Specialist Committee on Hydrodynamic Noise*, 2017.

[15] J.-P. Franc and J.-M. Michel, *Fundamentals of cavitation*, vol. 76. Springer science & Business media, 2006.

[16] D. Wittekind and M. Schuster, "Propeller cavitation noise and background noise in the sea," *Ocean Engineering*, vol. 120, pp. 116–121, 2016.

[17] P. Pennings, J. Westerweel, and T. van Terwisga, "Cavitation tunnel analysis of radiated sound from the resonance of a propeller tip vortex cavity," *International Journal of Multiphase Flow*, vol. 83, pp. 1–11, 2016.

[18] C. Park, H. Seol, K. Kim, and W. Seong, "A study on propeller noise source localization in a cavitation tunnel," *Ocean Engineering*, vol. 36, no. 9-10, pp. 754–762, 2009.

[19] H. Yamaguchi, H. Kato, and K. Matsuda, "Measurement and computation of the acoustic field in a cavitation tunnel," *Journal of Marine Science and Technology*, vol. 1, no. 4, pp. 198–208, 1996.

[20] "7.5-02-01-05, model-scale propeller cavitation noise measurements," *ITTC Quality System Manual, Recommended Procedures and Guidelines*, 2017.

[21] F. Miglianti, F. Cipollini, L. Oneto, G. Tani, and M. Viviani, "Model scale cavitation noise spectra prediction: Combining physical knowledge with data science," *Ocean Engineering*, vol. 178, pp. 185–203, 2019.

[22] "Second international workshop on cavitating propeller perfomance." http://www.caee.utexas.edu/smp15/smp_workshop_2015.html. 2015.

[23] G. Kuiper, "New developments around sheet and tip vortex cavitation on ships propellers," *http://resolver. caltech. edu/cav2001: lecture. 007*, 2001.

[24] F. R. Menter, "Two-equation eddy-viscosity turbulence models for engineering applications," *AIAA journal*, vol. 32, no. 8, pp. 1598–1605, 1994.

[25] Siemens Digital Industries Software, *Simcenter Star-CCM+ Documentation, v15.06.008-r8*. Siemens, 2020.

[26] F. Menter and T. Esch, "Elements of industrial heat transfer predictions," in *16th Brazilian Congress of Mechanical Engineering (COBEM)*, vol. 109, p. 650, 2001.

[27] F. R. Menter, M. Kuntz, and R. Langtry, "Ten years of industrial experience with the sst turbulence model," *Turbulence, heat and mass transfer*, vol. 4, no. 1, pp. 625–632, 2003.

[28] M. Popovac and K. Hanjalic, "Compound wall treatment for rans computation of complex turbulent flows and heat transfer," *Flow, turbulence and combustion*, vol. 78, no. 2, p. 177, 2007.

[29] M. L. Shur, P. R. Spalart, M. K. Strelets, and A. K. Travin, "A hybrid rans-les approach with delayed-des and wall-modelled les capabilities," *International Journal of Heat and Fluid Flow*, vol. 29, no. 6, pp. 1638–1649, 2008.

[30] P. Perali, T. Lloyd, and G. Vaz, "Comparison of urans and bem-bem for propeller pressure pulse prediction: E779a propeller in a cavitation tunnel," in *Proceedings of the 19th Numerical Towing Tank Symposium, Nantes, France*, 2016.

[31] G. H. Schnerr and J. Sauer, "Physical and numerical modeling of unsteady cavitation dynamics," in *Fourth international conference on multiphase flow*, vol. 1, ICMF New Orleans, 2001.

[32] R. B. Langtry and F. R. Menter, "Correlation-based transition modeling for unstructured parallelized computational fluid dynamics codes," *AIAA journal*, vol. 47, no. 12, pp. 2894–2906, 2009.

[33] R. B. Langtry, "A correlation-based transition model using local variables for unstructured parallelized cfd codes," 2006.

[34] M. Ge, "Improve sheet cavitation inception prediction by taking laminar separation into consideration," in *Proceedings of CFD with OpenSource Software, Edited by Nilsson. H.*, 2018.

[35] S. Gaggero, "Influence of laminar-to-turbulent transition on model scale propeller performances. part ii: cavitating conditions," *Ships and Offshore Structures*, pp. 1–20, 2020.

[36] J. Ffowcs-Williams and D. Hawkings, "Sound generated by turbulence and surfaces in aroitrary motion," *Philosophical Transactions of the Royal Society (London) A*, vol. 264, p. 1969, 1969.

[37] F. Farassat and G. P. Succi, "A review of propeller discrete frequency noise prediction technology with emphasis on two current methods for time domain calculations," *Journal of Sound and Vibration*, vol. 71, no. 3, pp. 399–419, 1980.

[38] K. S. Brentner, "Prediction of helicopter rotor discrete frequency noise: A computer program incorporating realistic blade motions and advanced acoustic formulation," *Unknow*, 1986.

[39] F. Farassat, "Derivation of formulations 1 and 1a of farassat," tech. rep., 2007.

[40] "First international workshop on cavitation and propeller performance." https://www.sva-potsdam.de/smp11-propeller-workshop. 2011.

[41] J.-P. Franc and J.-M. Michel, "Attached cavitation and the boundary layer: experimental investigation and numerical treatment," *Journal of Fluid Mechanics*, vol. 154, pp. 63–90, 1985.

[42] J. H. Van der Meulen, "Boundary layer and cavitation studies of naca 16-012 and naca 4412 hydrofoils," in *Proceedings of 13th Symposium on Naval Hydrodynamics, Tokyo, Japan*, pp. 195–219, 1980.

[43] J. English, "Cavitation induced hull surface pressures–measurements in a water tunnel," 1980.

[44] A. Konno, K. Wakabayashi, H. Yamaguchi, M. Maeda, N. Ishii, S. Soejima, and K. Kimura, "On the mechanism of the bursting phenomena of propeller tip vortex cavitation," *Journal of marine science and technology*, vol. 6, no. 4, pp. 181–192, 2002.